UNIVERSITY OF TURKU

Hydrogens effect on materials used in Internal Combustion Engine (ICE) components

Mechanical engineering/Faculty of Technology
Master's thesis
Department of Mechanical and Materials Engineering

Author:
Tino Heikkilä

16.02.2026
Turku

Master's thesis

Subject: Mechanical engineering
Author: Tino Heikkilä
Title: Hydrogens effect on materials used in Internal Combustion Engine (ICE) components
Supervisors: Prof. Ashish Ganvir (UTU) and M.Sc.(tech) Visa Lang (Wärtsilä)
Number of pages: 72 pages
Date: 16.02.2026

Hydrogen has a negative effect on most metallic materials. The main mechanism for the negative effects is hydrogen embrittlement (HE). Hydrogen diffuses to the material's different microstructural features and defects, affecting the materials' mechanical properties by lowering the material's strength and toughness. Knowledge of material properties are crucial information in design and analysis for Internal Combustion Engines (ICEs) components.

This thesis will test two ICE component materials to see how the hydrogen affects their mechanical properties. These materials are X40CrSiMo 10-2 and 42CrMo4. The focus will be on the difference of tensile strength and strain of the material with and without hydrogen. The fracture surfaces were analysed to see how the hydrogen affected the fracture type. These both will be used to determine how much hydrogen has affected the materials.

The hydrogen experiments were conducted by the University of Oulu. These included machining of samples, hydrogen doping, and tensile testing. The reduction in mechanical properties was mostly on the strain and toughness of the materials. The reduction in strain for X40CrSiMo 10-2 was 60,2% and for 42CrMo4 52,1%. The toughness reduction was 67,7% and 54,9% respectively. Ultimate strength reduction was 6,7% and 3,3%. The fracture point's strength of X40CrSiMo 10-2 was reduced by 6,7% and for 42CrMo4 it increased by 10,3%.

Overall, the thesis concludes that both materials had a high reduction in strain and toughness due to hydrogen. Also, the strength of the materials was mostly reduced with one exception. These could be due to there only being one test per condition.

Keywords: Hydrogen embrittlement, Hydrogen embrittlement index, Mechanical properties, Internal combustion engine, Tensile strength, Stress, Strain

Diplomityö

Oppiaine: Konetekniikka
Tekijä: Tino Heikkilä
Otsikko: Hydrogens effect on materials used in Internal Combustion Engine (ICE) components
Ohjaajat: Prof. Ashish Ganvir (UTU) and DI Visa Lang (Wärtsilä)
Sivumäärä: 72 sivua
Päivämäärä: 16.02.2026

Vedyllä on negatiivinen vaikutus useimpiin metalleihin. Vetyhauras on suurin tekijä näihin negatiivisiin vaikutuksiin. Vety diffundoituu materiaalin mikrorakenteessa löytyviin eroihin ja virheisiin. Tämä vaikuttaa materiaalin mekaanisiin ominaisuuksiin alentamalla materiaalin lujuutta ja sitkeyttä. Tieto materiaalin ominaisuuksista on tärkeää polttomoottorien komponenttien suunnitellussa ja analyysissä.

Tässä diplomityössä testataa kuinka vety vaikuttaa kahden eri polttomoottori kompenentin materiaaleihin. Nämä materiaalit ovat X40CrSiMo 10-2 ja 42CrMo4. Painopisteenä oli vetolujuuden ja venymän muutos kun materiaali on altistettu vedylle. Myös murtopinnat tutkittiin, jotta nähtäisiin miten vety vaikutti materiaalin murtotyyppiin. Näitä tietoja käytetään määrittämään kuinka paljon vety vaikutti kyseisiin materiaaleihin.

Vety testaukset toteutettiin Oulun yliopistossa. Vety testauksiin kuului näytteiden koneistaminen, vety lataukset, ja vetokokeet. Mekaanisten ominaisuuksien lasku oli suurinta venymässä ja sitkeydessä. Venymän arvo laski materiaalilla X40CrSiMo 10-2 60,2% ja materiaalilla 42CrMo4 52,1%. Samojen materiaalien sitkeys laski 67,7% ja 54,9%. Murtolujuudet laskivat 6,7% ja 3,3%. Murtuma kohdan lujuus laski X40CrSiMo 10-2 materiaalilla 6,7% kun taas materiaalilla 42CrMo4 se nousi 10,3%.

Opinnäytetyön lopputulemana molempien materiaalien venymä ja sitkeys laski huomattavasti vedystä johtuen. Myös materiaalien lujuudet laskivat hieman ja yhdessä tapauksessa se nousi. Tämä voi johtua siitä, että testejä tehtiin vain yksi per olosuhde.

Avainsanat: Vetyhauraus, Vetyhauraus indeksi, Mekaaniset ominaisuudet, Polttomoottori, Vetolujuus, Jännitys, Venymä

Acknowledgements

I am grateful to everyone in Wärtsilä Turku investigation laboratory for their help and guidance before and during the thesis. Especially on the use of different testing equipment and the safe use of chemicals. I also extend my gratitude to Jonas Sundblom for his ideas on the thesis's contents, and comments and questions on the thesis's progress. I am also grateful to Visa Lang for obtaining the right to start my thesis on the topic that I was curious of, and for his comments on the thesis. I express my appreciation to Ashish Ganvir for his great courses on the more material science side of mechanical engineering, and for his help on the thesis process.

Table of contents

List of Figures

List of Tables

Nomenclature

Abbreviation	Explanation
BDC	Bottom Dead Centre
BSE	Backscattered electrons
DT	Destructive testing
EDS	Energy Dispersive Spectroscopy
HE	Hydrogen embrittlement
HEDE	Hydrogen-enhanced decohesion mechanism
HEE	Hydrogen environment embrittlement index
HEI	Hydrogen embrittlement index
HELP	Hydrogen-enhanced localized plasticity
HESIV	Hydrogen-enhanced strain-induced vacancies
HIPT	Hydrogen-induced phase transfer theory
ICE	Internal Combustion Engine
MVC	Microvoid coalescence
NDT	Non-destructive testing
NVC	Nanovoid coalescence
OES	Optical Emission Spectroscopy
PRHIC	Plasticity-related hydrogen induced cracking
QP	Quenched and partitioned
QT	Quenched and tempered
SE	Secondary electrons
SEM	Scanning Electron Microscope
SSRT	Slow strain rate testing
TDC	Top Dead Centre
UTS	Ultimate tensile strength

1 Introduction

1.1 Background for the thesis

The idea for the thesis came from me as my Batchelor's thesis topic which was about green fuels effects on laser powder bed fusion metals. Also, there was interest in knowing how, and how much hydrogen affects certain components on internal combustion engines (ICEs). As, some of the component's materials have not been studied before. Studies with similar microstructures have been made but the exact effect on the certain type and chemical composition of the material could not be found. The effects could change due to different manufacturing processes used or chemical composition.

The purpose of this thesis was to gather data for research and development, and to prepare the failure analysis teams on the potential further use of hydrogen as a fuel. The analysis of the fracture surfaces could also help in identifying other phenomena in which hydrogen could be trapped/diffused to metals. As some manufacturing processes can trap and help hydrogen to diffuse to the metal materials.

1.2 Research problem and research questions

Hydrogen is starting to be adopted as an alternative fuel in many fields to combat greenhouse gas emissions. Challenges with hydrogen as fuel in ICEs, introduces the effects of hydrogen on the components of the ICEs, the main critical challenge being hydrogen embrittlement (HE). There have been studies on the hydrogen embrittlement of many ICE component materials, but some of the component materials and mitigation strategies have not been tested. This research aims to quantify the effect of hydrogen on 42CrMo4 and X40CrSiMo 10-2 martensitic steels for ICEs, via mechanical testing after hydrogen doping of the samples. Also, it will look at the effects of the engine conditions (pressure and heat) on the hydrogen absorption in the literature review part as these cannot be tested quantitively due to budget restraints.

The key research questions for the thesis are:

- How the hydrogen exposure affects the selected materials mechanical properties/performance?
- How does the 42CrMo4 alloys test results compare to other studies results?

- Could the effect of hydrogen be mitigated in any way on the materials?
- How the fracture type of components material change when the material has been exposed to hydrogen?

1.3 Thesis scope and objectives

The scope of the thesis is to quantitively and qualitatively evaluate the effect of hydrogen on the ICEs component materials. This will include material selection for the tests and preparation of the samples from these materials. Hydrogen doping of the samples with electrochemical charging. Tensile testing will be done ex-situ i.e. after the electrochemical charging, to look at the loss of ductility and strength. The microstructure of the samples will be checked with etching and metallographic microscope. Fractography of the samples will be looked at using Scanning Electron Microscopy (SEM) and Energy Dispersive Spectroscopy (EDS) to determine the effects of hydrogen on the fracture type of the sample's materials. The results from the materials tensile testing will be quantitively analyzed and compared to data collected from different studies. The objectives for the thesis are to gather data on the effect of hydrogen environment on the ICE materials. Also, to see if the components' materials are compatible for use in hydrogen powered ICEs.

1.4 Structure of the thesis

The thesis is structured as follows:

- Chapter 1 introduction to the thesis background, scope, objectives and structure.
- Chapter 2 a literature review of hydrogen embrittlement and its testing methods.
- Chapter 3 methodology of the experimental work done for the thesis: hydrogen charging parameters, tensile testing parameters, sample preparation, equipment used, and analysis methods for data gathered from tensile testing and fractography.
- Chapter 4 going through the test results and the data gathered with the defined analysis methods and discussion based on the results. Also, looking at the results from an overall engineering standpoint i.e., whether the materials are suitable to be used in hydrogen ICEs. The possible future development ideas are also discussed.
- Chapter 5 concludes the thesis as a study and the beforementioned chapters.

2 Literature review

2.1 Hydrogen

Hydrogen is used as a fuel source in many different fields. These are automotive, aerospace, and marine. It has been shown to be used in ICEs and fuel cells. The aim for the use of hydrogen as a fuel source in different fields is to lower greenhouse gas emissions. As, there is a global effort to reach net zero emissions by 2050 [1], [2]. Hydrogen is stored in gas or liquid form. The volumetric energy density of hydrogen changes depending on the temperature, pressure, and form on which it is stored. In Figure 1 are different volumetric energy densities for common fuels and hydrogen. In liquid state the hydrogen is stored at cryogenic temperatures at 20K which is around -253°C in atmospheric pressure [3]. These bring challenges with material selection on the storage and transportation of hydrogen. Hydrogen is used in 4-stroke ICEs and more specifically in spark ignition engines [4].

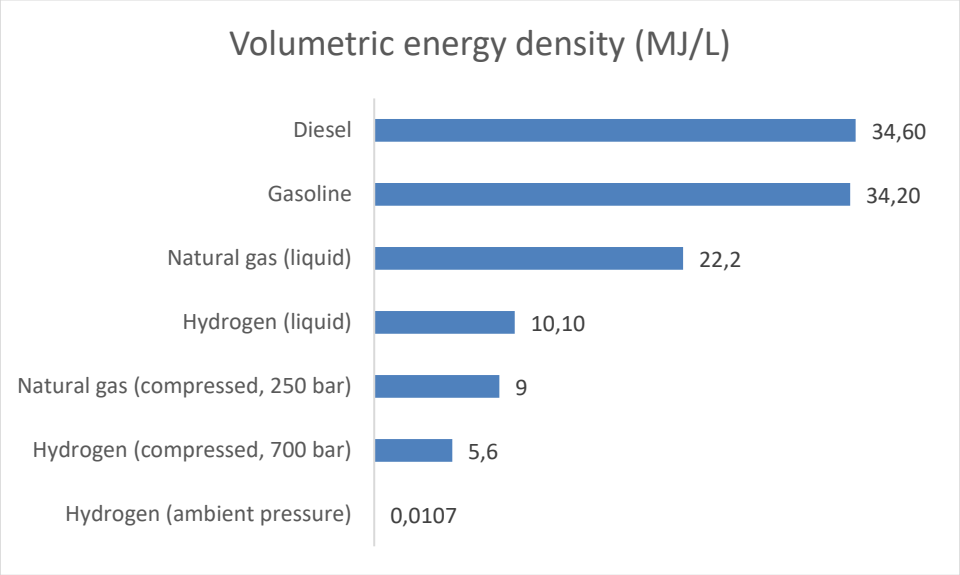

Figure 1 Volumetric density of common fuels used in ICES. [3], [5]

2.2 Internal combustion engine (ICE)

Internal combustion engine (ICE) is a heat engine where combustion of air and fuel mixture takes place in a combustion chamber. In which the expansion due to the combustion of the mixture results in direct force to the piston or rotor of the ICE leading to rotation force out from the driveshaft. [6]

2.2.1 Four-stroke cycle

Otto and Diesel ICEs use a four-stroke cycle which has four different stages: intake stroke, compression stroke, expansion/power stroke, and exhaust stroke, which are shown in Figure 2. [7]

1. Intake stroke starts when the piston is at the topmost point inside the cylinder i.e. it is at the Top Dead Centre (TDC). When the piston moves down the cylinder it draws in air/fuel mixture or fresh air, as the volume in the combustion chamber increases. [7]

2. Compression stroke starts when the piston has moved to Bottom Dead Centre (BDC) and the intake stoke has stopped. When the BDC is hit the intake valves close and the piston starts to move upwards towards the TDC staring to compress the mixture inside thus rising temperature and pressure. [7]

3. Expansion/power stroke, in Otto engine, slightly before the piston hits TDC the spark plug ignites the air and fuel mixture i.e. these types of engines are known as spark ignition engines. In Diesel engines the compression from the piston getting to TDC ignites the air and fuel mixture. Just after TDC the ignition of the mixture rapidly increases the temperature and pressure inside the cylinder which leads to expansion forces driving the piston down during the power stroke. [7]

4. Exhaust stroke, as the piston has been driven down to BDC by the power stroke and the cylinder is full of hot combustion/exhaust gases. Next the exhaust valves open to let the hot gases out and the pistons are moving towards the TDC pushing the gases out. As the piston gets closer to TDC the valves close and the cycle starts again from the intake stroke. [7]

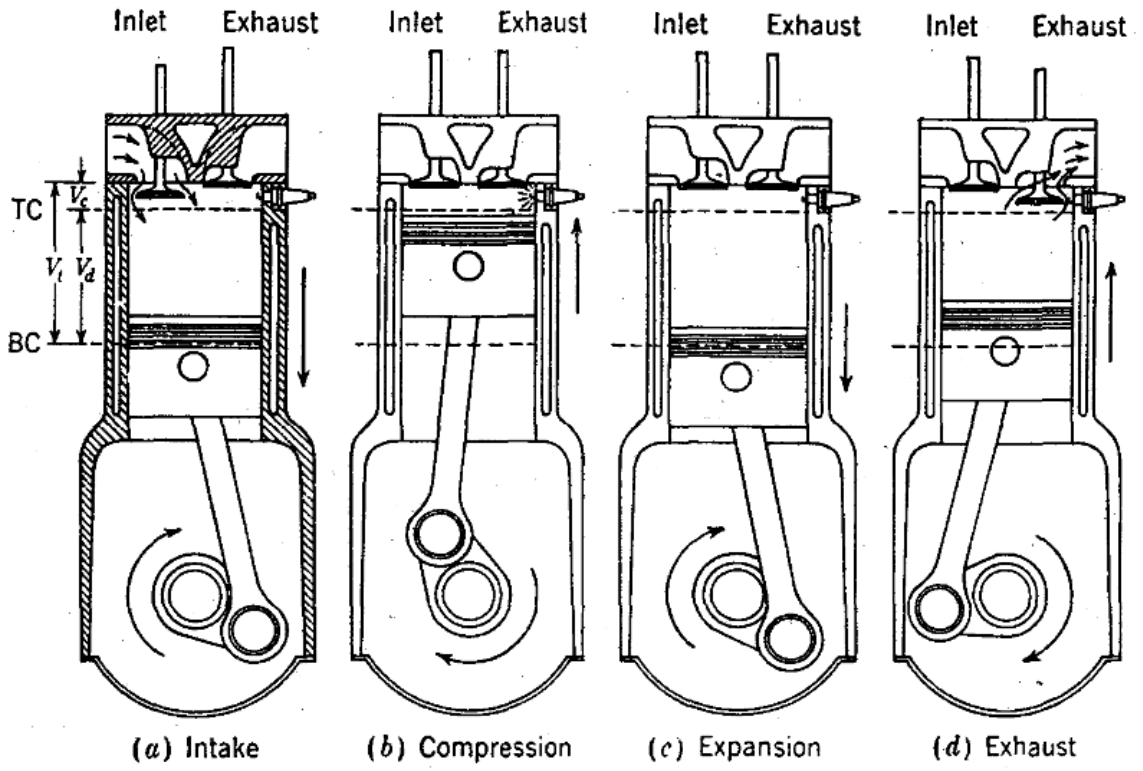

Figure 2 The four-stroke engines operating cycle schematic. (TC=TDC and BC=BDC) [7]

2.3 Failure analysis

Failure analysis is systematic and scientific research on how components or materials have failed or gotten damaged. The materials can be anything but in internal combustion engines they are mostly metals. Failure is broadly defined as the point in which the material or structure no longer can fulfill its function [8]. Understanding failures is a process which involves observing and analyzing the materials. Then applying engineering principles from different disciplines such as material science, manufacturing, thermodynamics, and others, to prevent future failures [9]. Also, it aims to identify different failure modes of components and how these failures affect the entire system. It has a significant role in research and development, warranty, and regulatory bodies, as some of the failures could lead to bodily harm and/or damage to property. Thus, it has a significant role in many different industries including marine, automotive, construction, and aerospace.

The analysis for failed components can be divided into two categories: Non-destructive testing (NDT) and destructive testing (DT). The names imply their modes of testing as NDT does not make changes to the tested material and is usually done before any destructive testing. These types of non-destructive tests include visual testing, dye penetrant testing, magnetic particle testing/inspection, X-ray fluorescence testing, ultrasonic testing, and

radiographic testing. They mostly only assess the surface of the component/material but some of the techniques can inspect the material under the surface. So, things that can be inspected are surface defects, wear characteristics, sub-surface defects, internal defects, metallic and non-metallic inclusions [10]. With x-ray fluorescence testing the materials bulk chemical composition can be obtained, and in ultrasonic and radiographic testing internal defects could be seen up to a certain point [10], [11]. In destructive testing the component is made into different samples, for example: machined into tensile testing specimens, Charpy V-notch specimens, and smaller pieces to fit it under SEM or other analyzers.

2.3.1 Tensile testing

Tensile testing shows how materials behave under applied stresses as the deformation and fracture characteristics of materials differ. The most common experimental method to test hydrogens effects on materials is tensile testing [12]. The focus will be on uniaxial load/tension, on the engineering tensile test as it provides basic information on the materials' strength. In this type of tensile testing the amount of uniaxial force is continually increased, and the elongation of the sample is simultaneously observed. [13]

The stress (s) on the sample is obtained by dividing load (P) with the original cross-section (A_0) seen in equation (1). The average linear strain (ε) i.e. the amount of deformation on the sample is calculated using the elongation (ΔL) of the sample by using the original length (L_0) and the current length (L) while the stress is applied the equation can be seen in (2). Strain rate is the change in strain (ε) per unit time equation (3). [13]

From these the engineering stress-strain curve can be obtained which can be seen in Figure 3. It shows the tensile strength (ultimate tensile strength) which shows the maximum amount of stress the material can withstand before necking or fracturing, and the amount of uniform strain on the material. Also, it shows offset yield strength point where the materials deformation has changed from elastic to plastic, and the dotted line shows how much it has permanently deformed as the point is after the yield point. Fracture stress shows the point where the material breaks and how much strain it gets before failure. This curve can also be modified to show relation with the engineering stress or stress, to the elongation. In slow strain rate testing the strain rate is slower compared to normal tensile testing. [13]

$$s = \frac{P}{A_0} \tag{1}$$

$$\varepsilon = \frac{\Delta L}{L_0} = \frac{L - L_0}{L_0} \quad (2)$$

$$\varepsilon' = \frac{\varepsilon}{t} \quad (3)$$

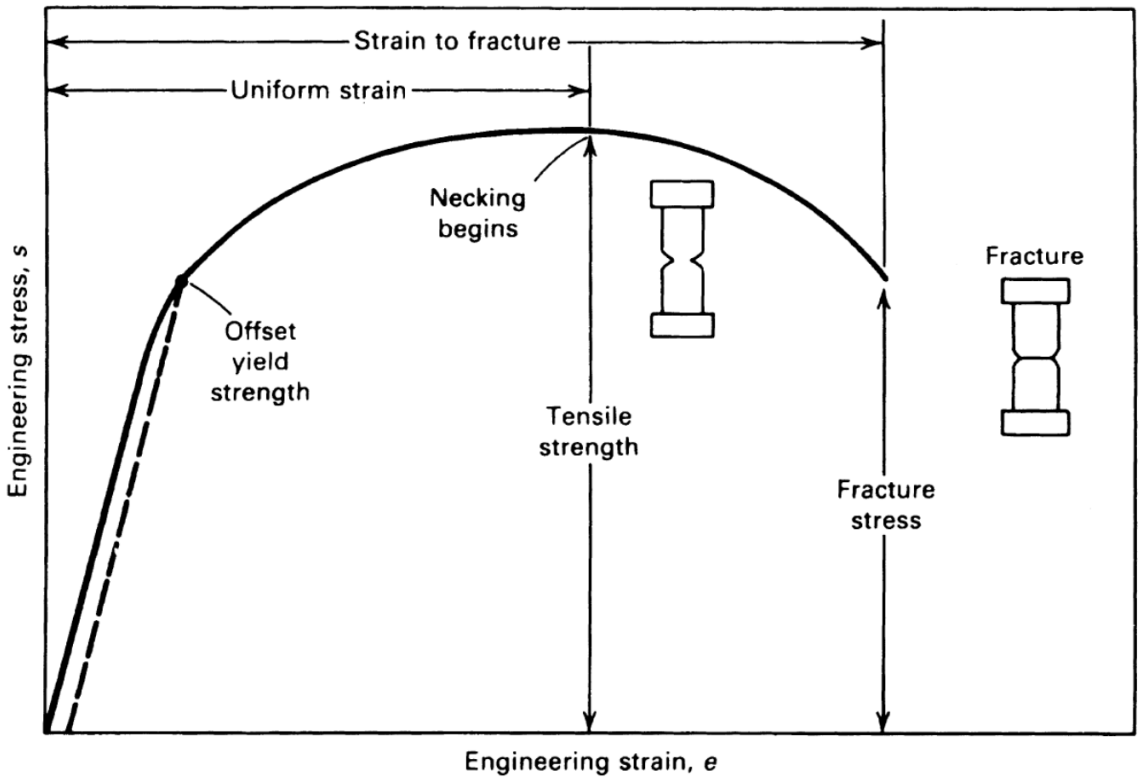

Figure 3 Engineering stress-strain curve. [13]

2.3.2 Fracture types

Fracture types are usually divided into two, brittle and ductile fractures. The effect of the fracture type on the stress-strain curve can be seen in Figure 4. In brittle fractures the toughness of the material i.e. the area under the curve is lower compared to ductile one. Toughness shows the amount of energy per area the material can absorb. Ductile materials can absorb more energy. Also, usually the strain and elongation of the material is lower in brittle materials. The fracture on brittle fractures usually happens before necking starts on the tensile testing sample.

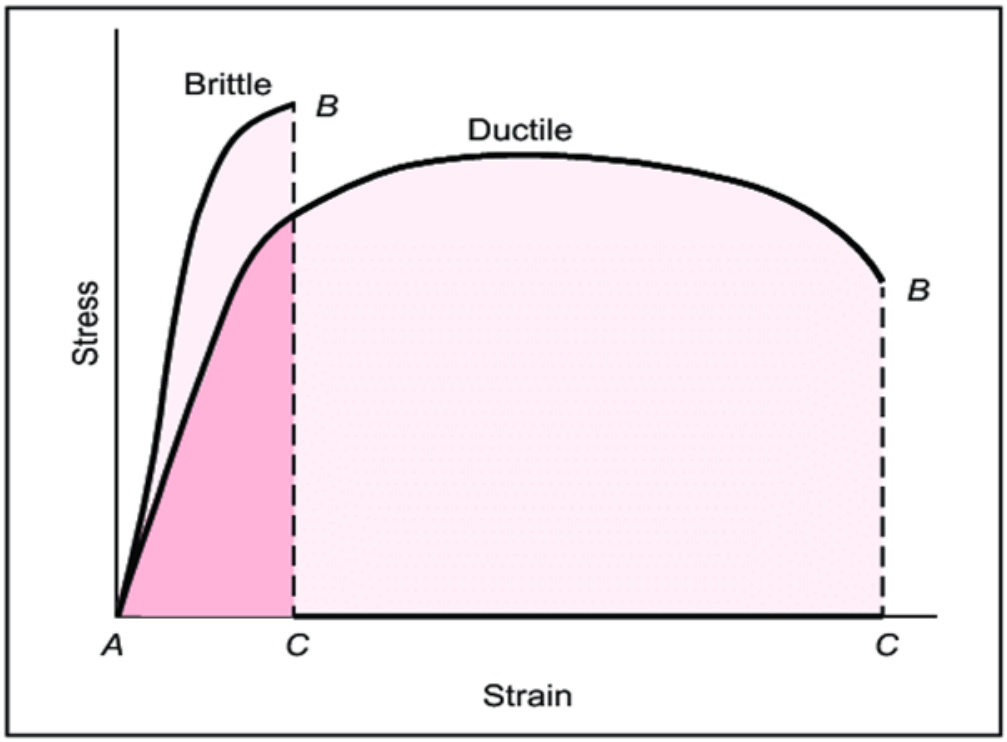

Figure 4 Stress strain curve for ductile and brittle fractures. [14]

Brittle fractures are usually categorized with intergranular and transgranular fracture mechanisms. In intergranular brittle fractures the fractures crack occurs at the grain boundaries. Usually, in transgranular brittle fractures the crack travels through the grain and not at the grain boundaries with sharper cleavage planes i.e. flat surfaces on the fracture surface. Intergranular fracture can be seen in Figure 5 showing a blocky like appearance and transgranular in Figure 6 showing the cleavage planes. [15]

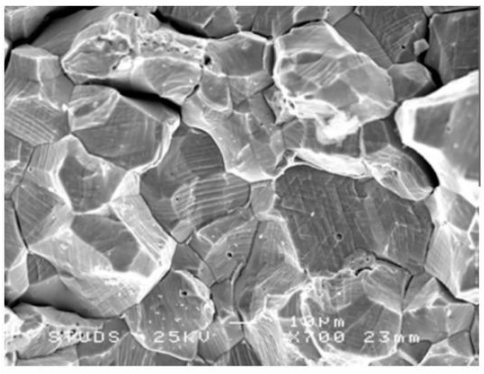

Figure 5 Intergranular fracture of A304 steel. [16]

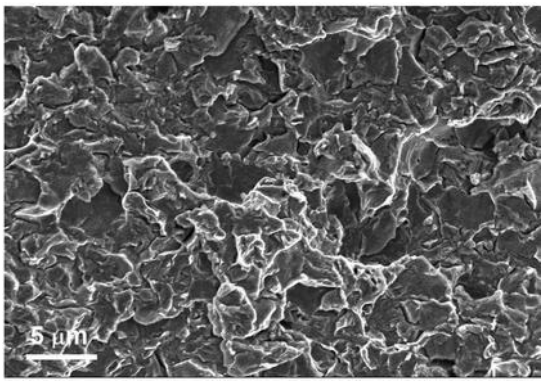

Figure 6 Transgranular fracture of ultra-high strength steel. Modified from [17].

Ductile fractures are usually identified from necking and for having dimples on the fracture surface. In microvoid coalescence (MVC) small voids in the material link together leading to a fracture during yielding of the material showing dimpled appearance. This type of fracture can be seen in Figure 7. [18]

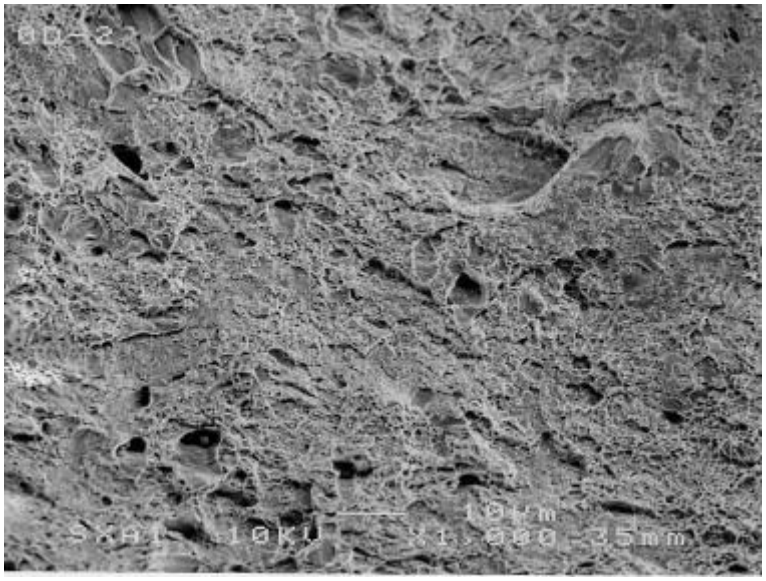

Figure 7 Conventional microvoid coalescence (MVC) showing the dimpled appearance. [19]

Fatigue fractures are caused by cyclic loading and usually start to form from imperfections in the metals and/or small cracks. These types of fractures can be identified from beach marks on the fracture surface. They usually point towards the imperfection that has started the fracture, this can be seen at the bottom in Figure 8.

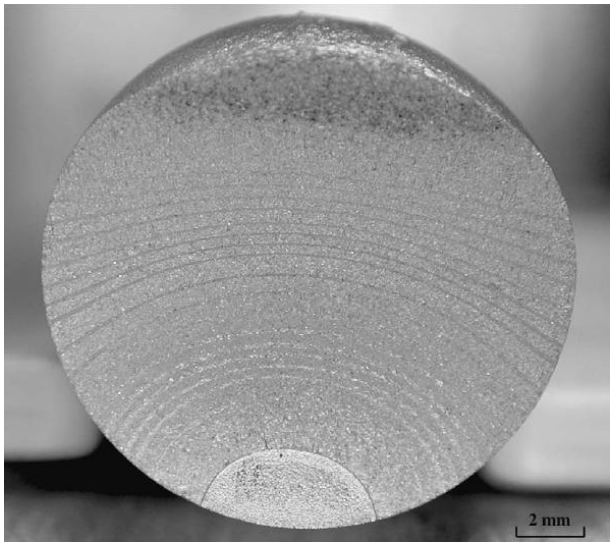

Figure 8 Fatigue fracture of a rod with beach marks. [20]

2.4 Hydrogen embrittlement (HE)

Phenomenon known as hydrogen embrittlement (HE) is due to the hydrogen being the smallest element and thus being able to penetrate and interact with metals. Leading to the degradation of their mechanical properties. Hydrogen embrittlement is a complex issue as the interaction between mechanical forces and material microstructures is affected by hydrogen. [12]

The subchapter looks at the different effects and transfer modes of hydrogen on metals.

2.4.1 Hydrogen absorption and diffusion

The hydrogens absorption, desorption, hydrogen fluxes inwards and outwards in the subsurface and the diffusion to the bulk can be seen in Figure 9. The difference of activation energies between the surface, subsurface, and bulk can be seen in Figure 10. In the model shown in Figure 9 the hydrogen atoms migrate from the surface to the subsurface from which it then diffuses to the bulk of it. The hydrogen content inside the bulk depends on the hydrogen fluxes between the interfaces at the surface and the subsurface. The fluxes are dependent on the activation energies, constants obtained from analysis or experiments, pressure, and temperature. [21]

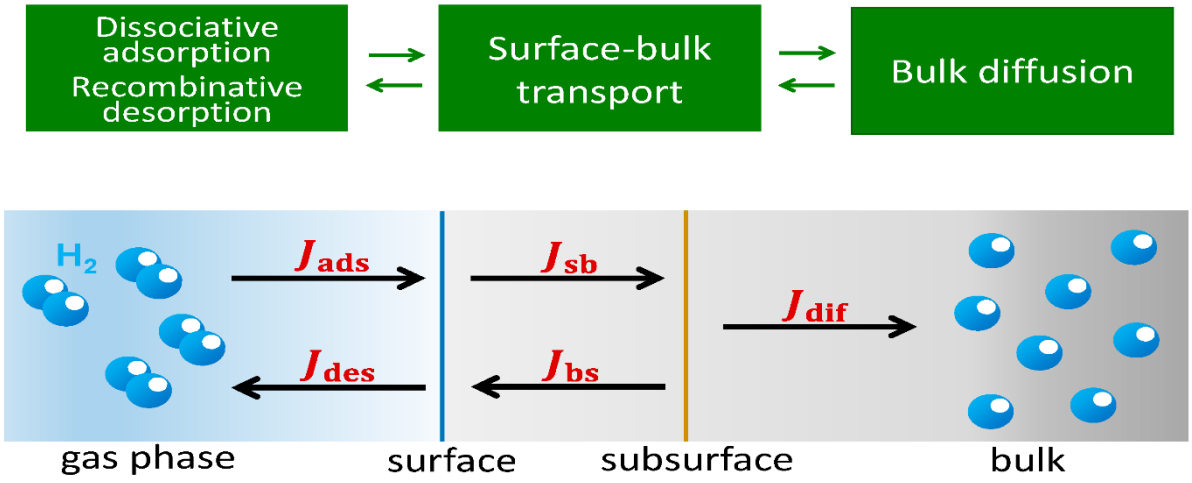

Figure 9 Schematic diagram of the hydrogens fluxes absorption (J_{ads}) and desorption (J_{des}), the hydrogen fluxes inwards (J_{sb}) and outwards (J_{bs}), and the diffusion to the bulk (J_{dif}). Modified from [21].

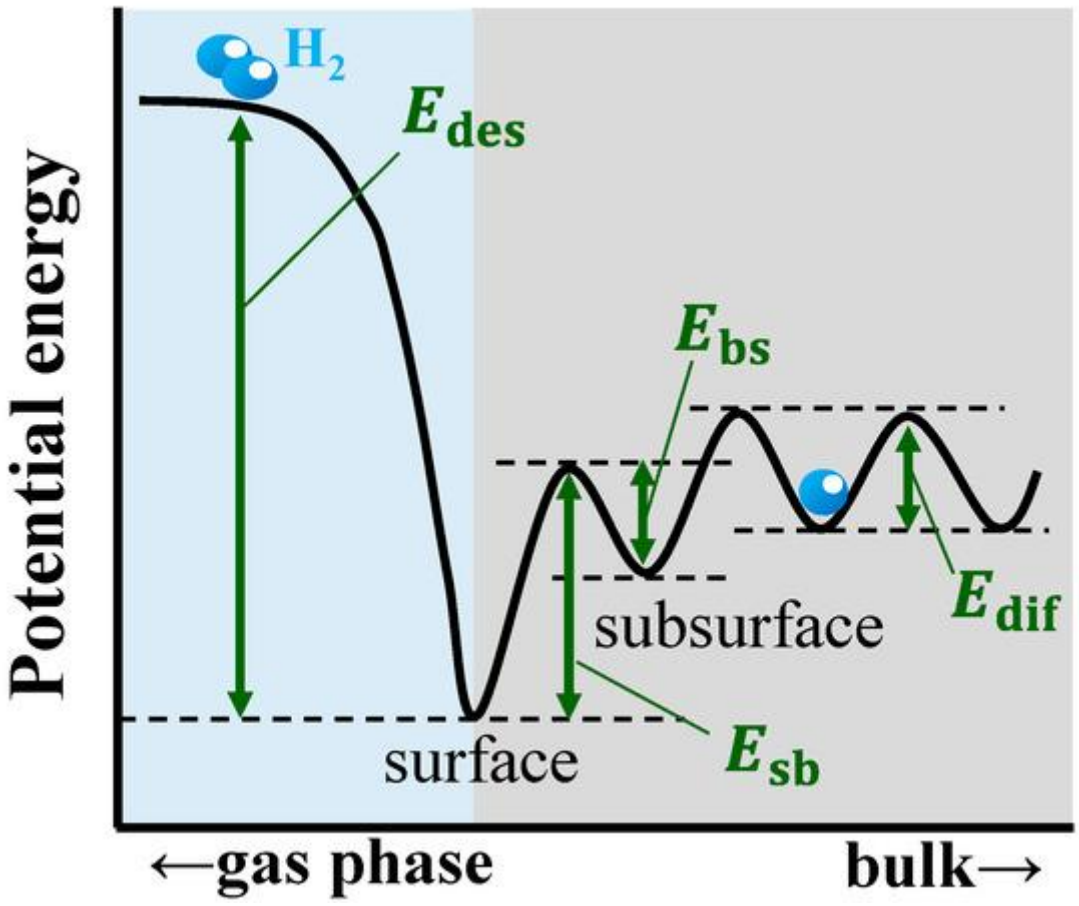

Figure 10 Schematic diagram of potential energies for hydrogen absorbing metals. E_{des} is the activation energy value for desorption, E_{sb} value for migration of hydrogen from the surface to subsurface, E_{bs} value for subsurface to surface migration, and E_{dif} value for diffusion of hydrogen into the bulk region. [21]

2.4.2 Trapping of hydrogen in steels

Hydrogen trapping is a phenomenon where hydrogen atoms are retained inside the material's microstructural defects during interstitial diffusion. The hydrogen absorbed by material in the crystalline structure can be in three different forms: diffused hydrogen, reversible trapped hydrogen and irreversibly trapped hydrogen [12]. The small hydrogen atoms can move/diffuse through interstitial sites i.e. small gaps between atoms in a solid crystal lattice.

Different types of traps for hydrogen on metals lattice can be seen in Figure 11. Hydrogen can be trapped in interstitial sites, surface traps, subsurface traps, grain boundaries, dislocations, and vacancies [22]. It can also be trapped in the interface between the base material and voids or inclusions left to the material after alloying and/or manufacturing processes. In Figure 12 the different trap sites are illustrated on a microscopic and lattice scale. Grain boundaries are the interface between two differently oriented crystals in a crystalline lattice of a material.

This is shown in Figure 11 by the difference in angle of the atoms and in Figure 12 by the small gray lines. Dislocations are line defects that are seen in all crystalline structures. The type of dislocation marked with ⊥ in Figure 11 is an edge dislocation where there is an incomplete plane of atoms within a crystal, the lower edge of it is shown at the bottom edge of the ⊥. Vacancies are point defects where an atom is missing from the normal lattice. [23]

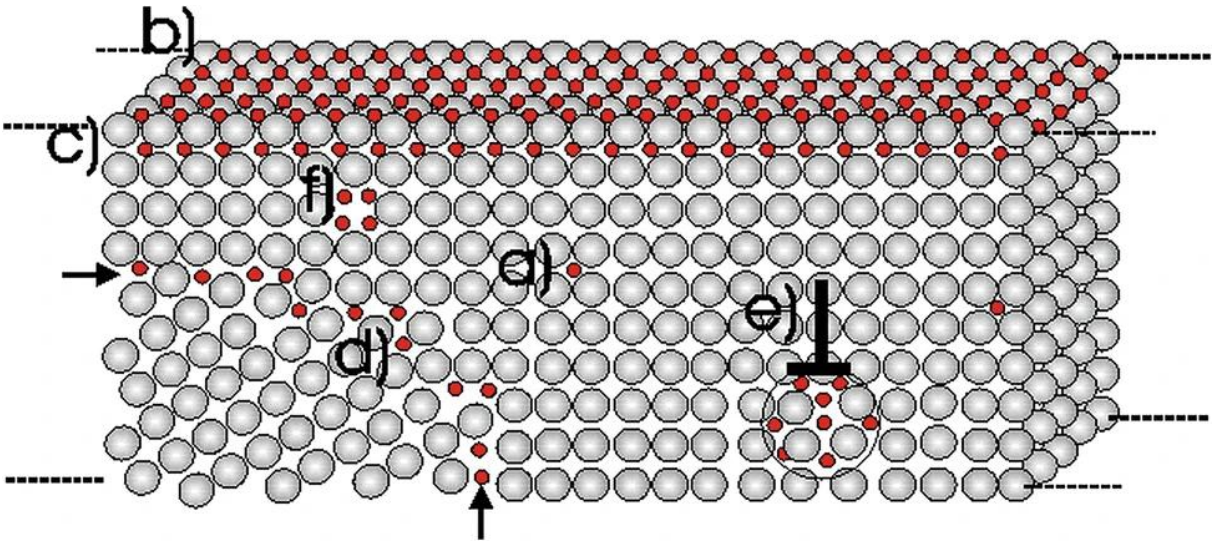

Figure 11 Hydrogen traps in steels lattice, a) interstitial sites, b) surface traps, c) subsurface traps, d) grain boundary traps, e) dislocation traps, f) vacancy traps. [22]

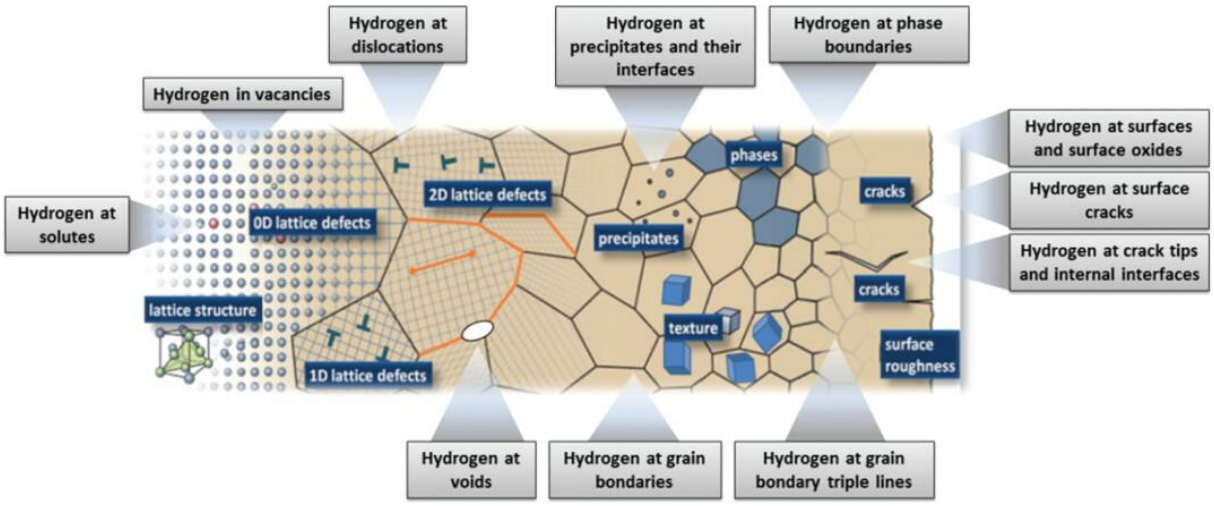

Figure 12 Illustration of trap sites for hydrogen on lattice and microscopic scale.[24]

The traps can be classified as irreversible and reversible. This classification is done by their binding energy/activation energy. They are classified as irreversible if the activation energy is higher than 60 kJ/mol, and as reversible if it is under it [22]. In Table 1 different types of traps and their activation energies are listed.

Table 1 Trap types and their binding / activation energies based on references ([22], [25]).

Trap type:	Binding energy / activation energy (kJ/mol)
Interstitial site in iron-based alloy	4 - 8
Lath boundary	~18
Austenite/martensite	22
Dislocation	24 - 26
Screw dislocation core	20 - 30
Grain boundary	18 - 53
Fe oxide interface	47
Ferrite/cementite interface	66 - 68
Cr carbide interface	67
Y_2O_3 interface	70
MnS interface	72
Al_2O_3 interface	79
Fe_3C interface	84

2.4.3 Hydrogen embrittlement mechanisms

There are many different theories on how hydrogen damage occurs in metal alloys. These damage types have been divided into two different categories by how the hydrogen is trapped. It can be trapped reversibly or irreversibly. Theories explaining the phenomenon of irreversibly trapped hydrogen damage are hydrogen pressure theory and hydrogen-induced phase transfer theory (HIPT). For reversible theories they are hydrogen-enhanced decohesion mechanism (HEDE), hydrogen-enhanced localized plasticity mechanism (HELP), and hydrogen-enhanced strain-induced vacancies (HESIV). From which not one has been universally accepted to account for all forms of reversible HE phenomena. Other mechanism theories for HE is Nanovoid coalescence mechanism (NVC), and combination of Hydrogen-enhanced decohesion mechanism (HEDE) and hydrogen-enhanced localized plasticity mechanism (HELP). All the mechanisms are based on postmortem i.e. after failure observations of samples. Thus, they do not provide direct evidence on the effect of the hydrogens on the cohesive strength and promotion of dislocation movement. [22]

Hydrogen pressure theory suggests that hydrogen atoms accumulate/segregate at defect location like micro voids and inclusion sites. These locally accumulated hydrogen atoms then

combine back to hydrogen molecules. When the process of hydrogen atoms being diffused to the metal continues. The amount of hydrogen molecules at these defect locations rise, producing a high hydrogen gas pressure. When this local pressure exceeds the materials critical strength, hydrogen-induced cracking takes place. Illustration of hydrogen-induced cracking at a defect location by the hydrogen pressure can be seen in Figure 13. [22]

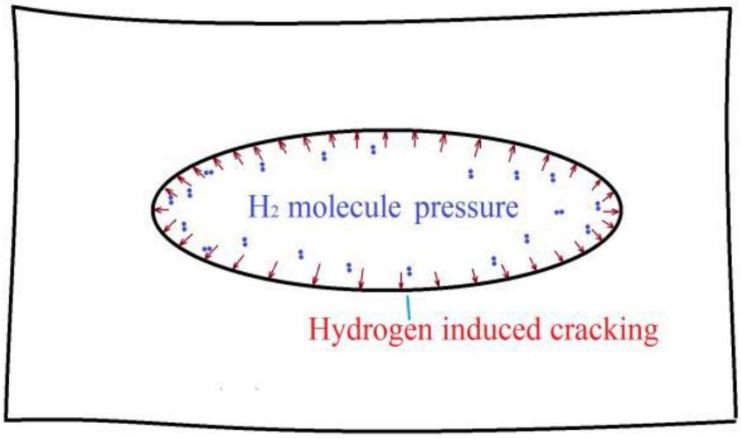

Figure 13 Hydrogen-induced cracking at a defect location with hydrogen pressure. [26]

Hydrogen-induced phase transfer theory (HIPT) illustrated in Figure 14, proposes that certain elements in alloys can form brittle hydrides due to their strong metal-hydrogen bonding energies. Some of these specific alloying elements are zirconium (Zr), niobium (Nb), vanadium (V), and tantalum (Ta). The formation of hydrides can be spontaneous, or stress induced. In spontaneous formation the hydrogen can directly combine with these specific metals at high hydrogen concentrations. In stress induced formation the local hydrogen concentration reaches the solubility level to the metal by the low hydrogen concentration being redistributed due to stress gradient field. The mechanism is divided into four steps seen in Figure 14. 1) Hydrogen diffuses and accumulates at the crack tip, 2) hydrides start to from and grow, 3) crack occurs along a specific cleavage plane within the brittle hydride, 4) crack propagation ends at the interface of the hydride and material. [22], [27]

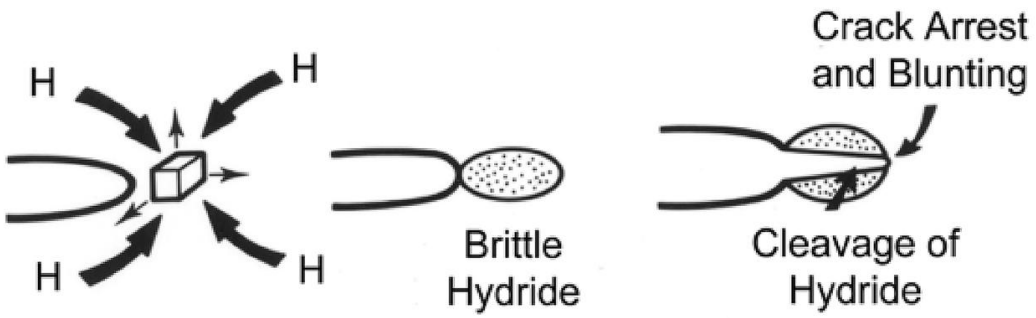

Figure 14 Schematic diagrams of Hydrogen-induced phase transfer theory (HIPT). Modified from [22]

Hydrogen-enhanced decohesion mechanism (HEDE) is illustrated in Figure 15, where the hydrogen reduces the cohesive interatomic interactions/bonds. In a way that atomic separation is more prone to happen under low tensile stress. This is due to the hydrogen being absorbed near the crack tip which in turn leads to weakening of the bonds between atoms, presumably metal bonds leading to brittle fracture. The weakening also contributes to the propagation and formation of dislocations. Also, hydrogen segregates at grain boundaries resulting in the reduction on the cohesive interactions between the metals' atoms in metal bonds. Due to this intergranular fractures have been seen in HEDE HE mechanisms. [12], [22], [27], [28], [29]

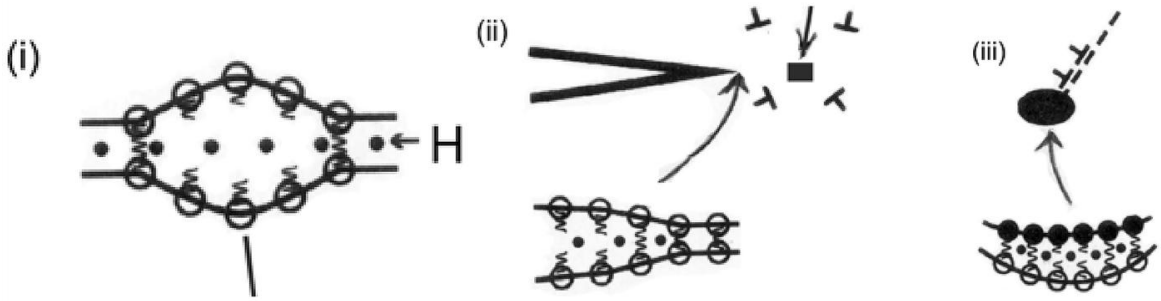

Figure 15 Schematic diagrams of Hydrogen-enhanced decohesion mechanism (HEDE). Modified from [22]

Hydrogen-enhanced localized plasticity mechanism (HELP) is illustrated in Figure 16, in which hydrogen promotes generation and mobility of dislocations. When hydrogen is in solid solution it affects the barrier for dislocation movement, thus causing enhanced localized deformation near the fracture surface. The interstitial hydrogen accumulates at the crack tip by dislocation-assisted convection and the concentration of it is higher in these localized deformation areas, which are designated as the HELP zone. These dislocation pileups in a localized area, contribute to premature material failure. It is also stated that the hydrogen atmosphere enhances dislocation mobility by the hydrogen segregating to the lattice defects like dislocations and reduces the strain energy in the area. When comparing HELP to HEDE,

HELP emphasizes the crucial role of alloy's plasticity in hydrogen-assisted fracture. In HELP the failure is not classified as embrittlement but rather as a highly localized plastic failure process due to the hydrogen. [22], [27], [28], [29], [30]

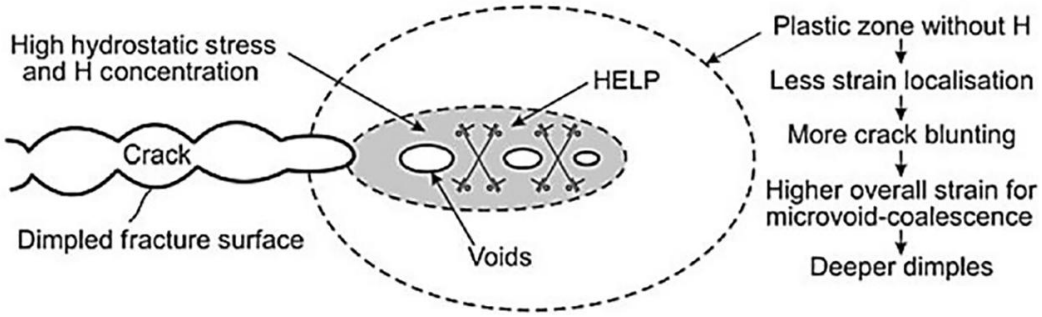

Figure 16 Schematic diagrams of Hydrogen-enhanced localized plasticity mechanism (HELP). Modified from [22]

Hydrogen-enhanced strain-induced vacancies (HESIV) mechanism is illustrated in Figure 17. In which it is assumed that hydrogen accelerates formation of strain-induced vacancies and stabilizes vacancy clusters. These vacancies clusters together are said to facilitate microvoids initiation and growth, and the linking of said microvoids speeds up the progression of ductile fracture. [22], [28]

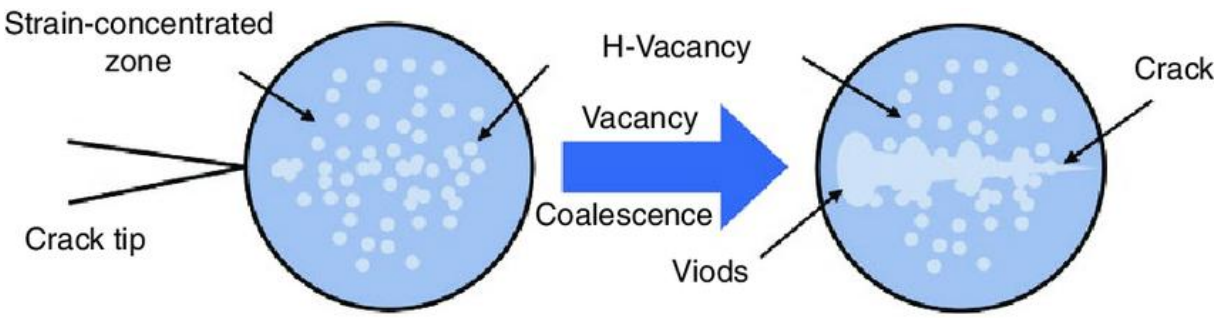

Figure 17 Schematic diagrams of Hydrogen-enhanced strain-induced vacancies (HESIV). [31]

Nanovoid coalescence mechanism (NVC) is illustrated in Figure 18. In the first stage deformation ahead of the crack tip starts generating dislocation plasticity. Thus, it can be said that it happens in accordance to HELP mechanism as the hydrogen accumulates at the crack tip by a dislocation-assisted convection. The localized plasticity by accumulation hydrogen leads to high local concentrations of hydrogen. These then leads to occurrence of intense plasticity on then second stage in regions with higher concentration of hydrogen very close to the crack tip. In stage three the dislocation plasticity generates and accumulates excess vacancies in the HELP zone which are being stabilized with hydrogen by binding to said vacancies. Stage four starts when critical local excess vacancy concentration is reached and

nanovoids start to nucleate and grow. This nucleation and growth lead to fracture by nanovoid coalescence. Typical fracture surface made by this type of HE mechanism is quasi-brittle densely covered with nano dimples. The stages show that NVC mechanism has effects from HEDE, HELP, and HESIV. [22], [28], [32]

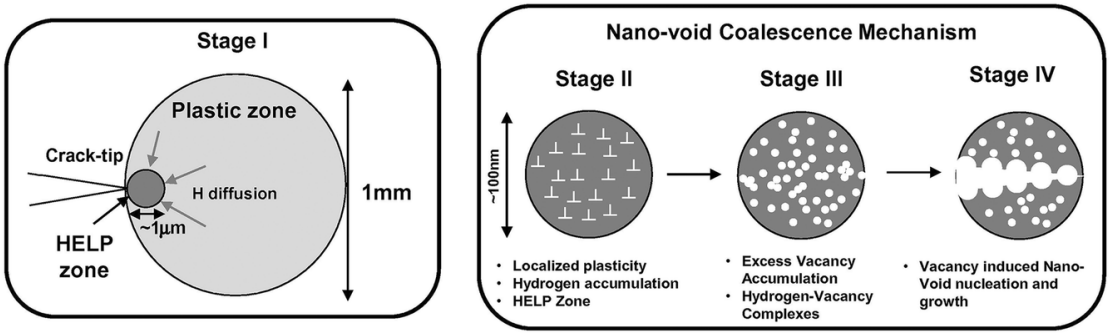

Figure 18 Schematic diagrams of Nanovoid coalescence mechanism (NVC). Modified from [22]

Hydrogen-enhanced decohesion mechanism (HEDE) and hydrogen-enhanced localized plasticity mechanism (HELP) combined effects illustrated in Figure 19. Similarly to NVC at in the first stage deformation ahead of the crack tip starts generating dislocation plasticity and hydrogen accumulates at the crack tip by a dislocation-assisted convection. The localized plasticity by accumulating hydrogen leads to high local concentrations of hydrogen. On second stage the accumulated hydrogen induces local plasticity and weakens the HELP zone. Which in stage three leads to decohesion reducing the cohesion between metal bonds leading to fracture. [12], [22]

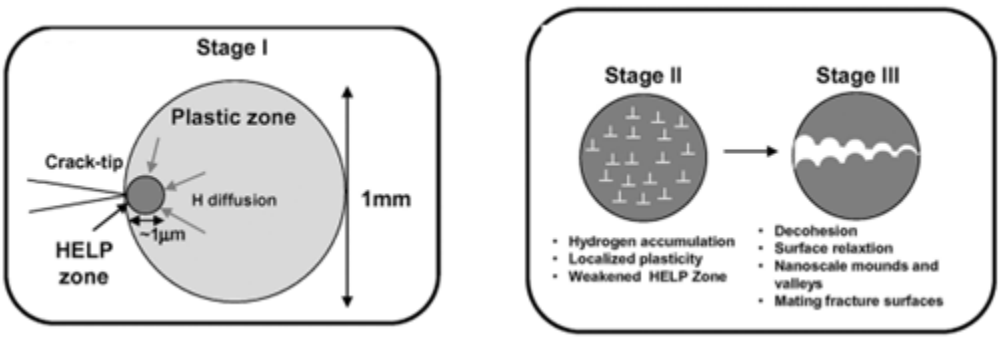

Figure 19 Schematic diagrams of Hydrogen-enhanced decohesion mechanism (HEDE) and hydrogen-enhanced localized plasticity mechanism (HELP) combined effects. Modified from [22]

2.4.4 Hydrogen charging methods

Gaseous hydrogen charging is done with pressurized hydrogen. There are autoclaves and high-pressure reactors that can vary the temperature together with the hydrogen pressure. Also, pressurized chambers are used to precharge samples before tensile testing, and there are testing machines that can do tensile testing in a pressurized chamber. Cathodic/ electrochemical hydrogen charging is done in an acidic aqueous medium which is commonly known as an electrolyte. Hydrogen is made from the electrolyte through electrolysis in which external current is flown through the sample acting as a cathode and a platinum electrode acting as the anode. Most used electrolytes consist of water with addition of sodium chloride (NaCl), sodium hydroxide (NaOH), and/or H_2SO_4. The most used electrolyte for the electrochemical charging of martensitic steels is H_2SO_4 together with As_2O_3 which is used to prevent hydrogen recombination from H^+ ions to gaseous hydrogen H_2. Thiourea can also be used to prevent the recombination. Also, there is a variable called current density which affects the concentration of hydrogen inside the sample but most used one is $1mA/cm^2$. [12], [22]

2.4.5 Hydrogen embrittlement's effect on mechanical properties

Hydrogen has been shown to affect metals tensile strength (ultimate tensile strength), ductility, toughness, and fatigue toughness [22]. It affects all metal alloys, but some are more resistant to it than others. In Table 2 are comparison between different alloys and ratios of strength, elongation, and reduction in area between charged and non-charged samples. Strength ratios are gathered from notched tensile tests, and elongation and reduction in area from smooth ones. The severity is based on these ratios and are as follows, negligible 1,0 – 0,97, small 0,96 – 0,90, high 0,89 – 0,70, severe 0,69 – 0,50, and extreme 0,49 – 0,0. These are hydrogen environment embrittlement (HEE) index values. Hydrogen embrittlement index (HEI) is calculated with equation (4), and in which the X_h is the material property with hydrogen and X_f is the property without hydrogen. The preferred values for the severity ratings are the strength and reduction in area ratios. [33]

$$HEI = \frac{X_f - X_h}{X_f} * 100\% = (1 - HEE) * 100\% = \left(1 - \frac{X_h}{X_f}\right) * 100\% \quad (4)$$

Table 2 Table of different metal alloys and their ratios of strength, elongation, and reduction in area between hydrogen charged and non-charged samples. [33]

Severity	Material	Microstructure categorization	Strength ratio H_2/He	Elongation ratio H_2/He	Reduction in area ratio H_2/He
Negligible	6061-T6	Aluminium based	1,07	1,00	1,08
	Copper (OFHC)	Copper based	1,00	1,00	1,00
	SS 316	Austenitic steel	1,00	0,95	0,96
	2024	Aluminium based	-	0,95	0,97
	22-13-5 (Nitronic 50)	Austenitic steel	-	1,00	1,00
Small	Titanium (pure)	Titanium based	0,95	0,96	1,00
	Be-Cu alloy 25	Copper based	0,93	1,00	0,98
	SS 310	Austenitic steel	0,93	1,00	0,96
	SS 347*	Austenitic steel	0,92	1,00	1,00
High	SS 304L	Austenitic steel	0,87	0,92	0,91
	4140 normalized	Ferritic steel	0,85	-	-
	Inconel® 718 no aging*	Titanium based	0,83	-	-
	Nickel 270	Nickel based	0,70	0,92	0,75
	X42	Ferritic steel	-	0,95	0,78
Severe	430F	Ferritic steel	0,68	0,63	0,58
	Ti-6Al-4v (STA)	Titanium based	0,58	0,85	0,95
	Inconel® 718 aged*	Titanium based	0,54	-	-
	X100*	Ferritic steel	-	0,63	0,49
	18-2-12 (Nitronic 32)	Austenitic steel	-	0,64	0,47
Extreme	440C	Martensitic steel	0,50	-	-
	4140	Ferritic steel	0,40	0,18	0,18
	4140 QT	Ferritic steel	0,25	0,19	0,19
	410	Martensitic steel	0,22	0,12	0,19
	440A	Martensitic steel	0,21	-	-
* At lower hydrogen pressure					

Two differently alloyed austenitic stainless steel (SS) 316, precharged with 138 MPa hydrogen gas at 573K for 10 days engineering stress and strain curve can be seen in Figure

20. These show that hydrogen charging has only a small effect on the mechanical properties of SS 316. Alloy E had more Nickel and Molybdenum compared to alloy A. [34]

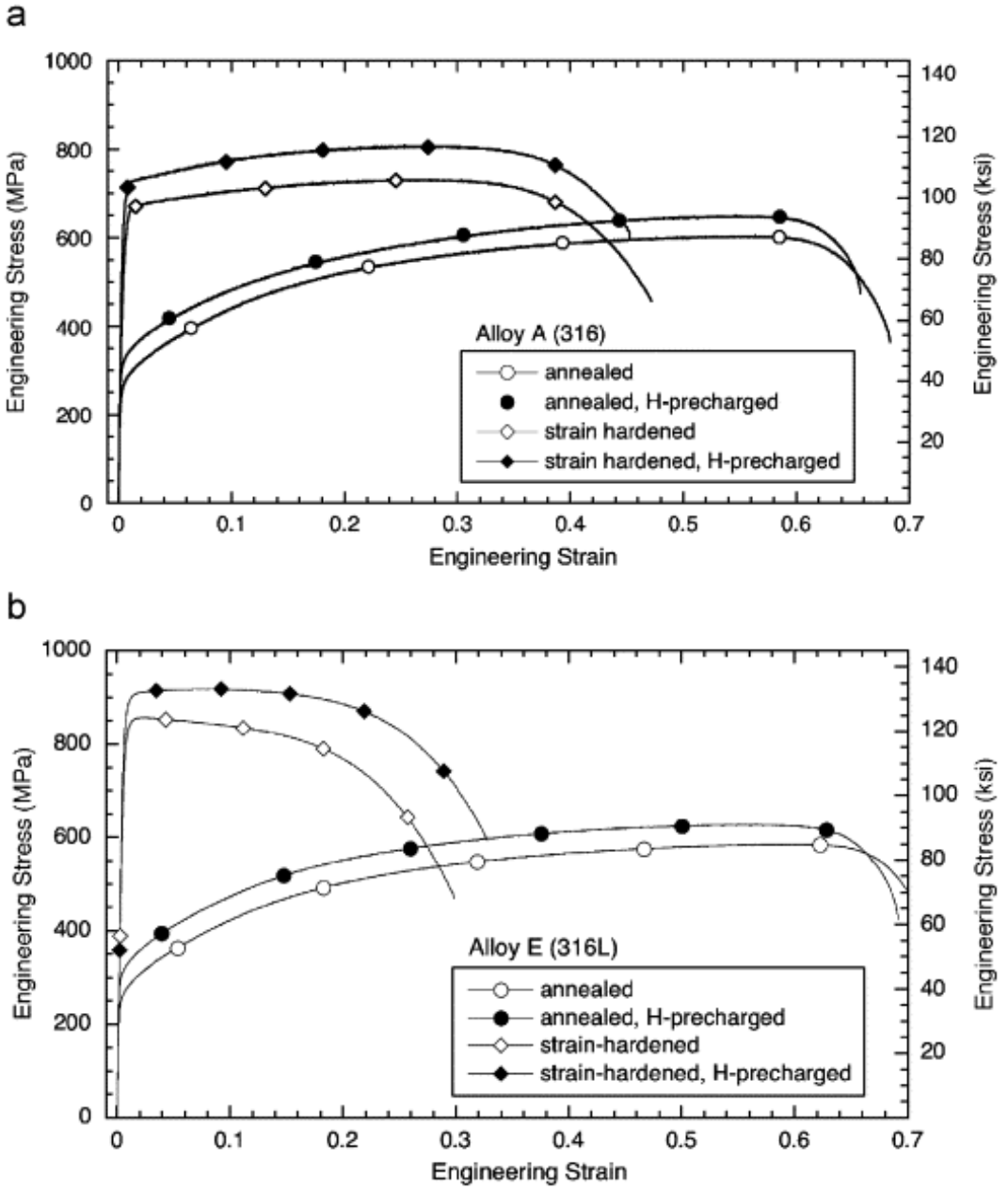

Figure 20 Engineering stress and strain curves for two differently alloyed SS 316. [34]

Stainless steels 310S, 304L, 410 were tested in air (a) and hydrogen (h) atmospheres. The 410A is air hardened and untempered, and 410T is tempered. They were tested with notched tensile testing. The hydrogen doping was done with hydrogen gas at 2MPa in-situ i.e. while the notched tensile tests were running. The notched tensile tests results can be seen in Figure 21, They were done in different temperatures 25°C (Figure 21a) and 80°C (Figure 21b). [35]

The results show that on 304L the higher temperature reduced the ultimate tensile strength (UTS) of the material at air atmosphere, and it was about the same on the different hydrogen atmospheres. For 304L the hydrogen affected its displacement and the change in displacement was higher at lower temperature. Alloy 310S had only minor changes in its strength and displacement values in both atmospheres. On 410A the higher air temperature showed a small lowering of its strength. In hydrogen atmosphere at lower temperature the strength was lower compared to the higher temperature. On 410T the displacement difference was slightly higher on the higher temperature. 304L and 310S had microstructure of equiaxed austenite with annealing twins. 410A and 410T had martensitic microstructure, 410A having untempered martensite and 410T tempered martensite. [35]

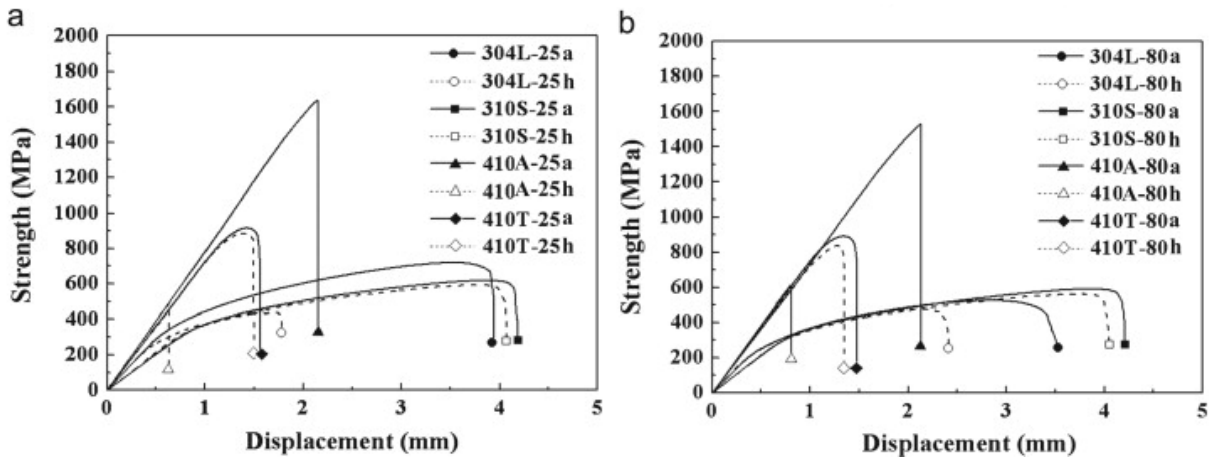

Figure 21 Strength and displacement curves for 304L, 310S, 410A, and 410T at different temperatures a) temperature was 25°C and in b) 80°C with atmospheres of air (a) and hydrogen (h). (modified from [35])

2.4.6 Temperatures, pressures, and times effect on hydrogen embrittlement

In the previous chapter the temperatures effect on a few stainless steels were also covered. It showed that the ratio of strength and displacement between hydrogen charged, and non-charged samples were lower or the same at room temperature when comparing to higher temperature. It is also stated in literature that hydrogen embrittlement susceptibility is at the highest near and in room/ambient temperature especially in ferritic steels, austenitic steels, and nickel based alloys [27], [29], [36], [37]. Hydrogen embrittlement susceptibility means the materials tendency to become brittle under hydrogen atmosphere thus affecting the materials' mechanical properties. The higher hydrogen embrittlement susceptibility at room temperature is said to be due to hydrogen being more diffusible at elevated temperatures which promotes desorption of hydrogen from materials. Also, the elevated temperature gains

enough energy for the hydrogen to escape from weaker traps to the bulk lattice i.e., interstitial sites. In Figure 22 hydrogens thermal desorption profiles for samples CD-P (ferrite/cementite lamella structure), MC-M (martensitic lath, with block and packet substructures within prior austenite grains), and HC-M (lenticular martensite with twins, lath martensite, and retained austenite). The Figure 22 shows that the first peak in desorption rate is at around 400K (127°C) and it was said that it had activation energy of around 34kJ/mol which is for weaker traps releasing the hydrogen. Second peak at 650K (377°C) for CD-P for 62 kJ/mol activation energy and at 600K (327°C) for HC-M for 43kJ/mol, indicating of other weaker traps with different activation energies. [22], [38]

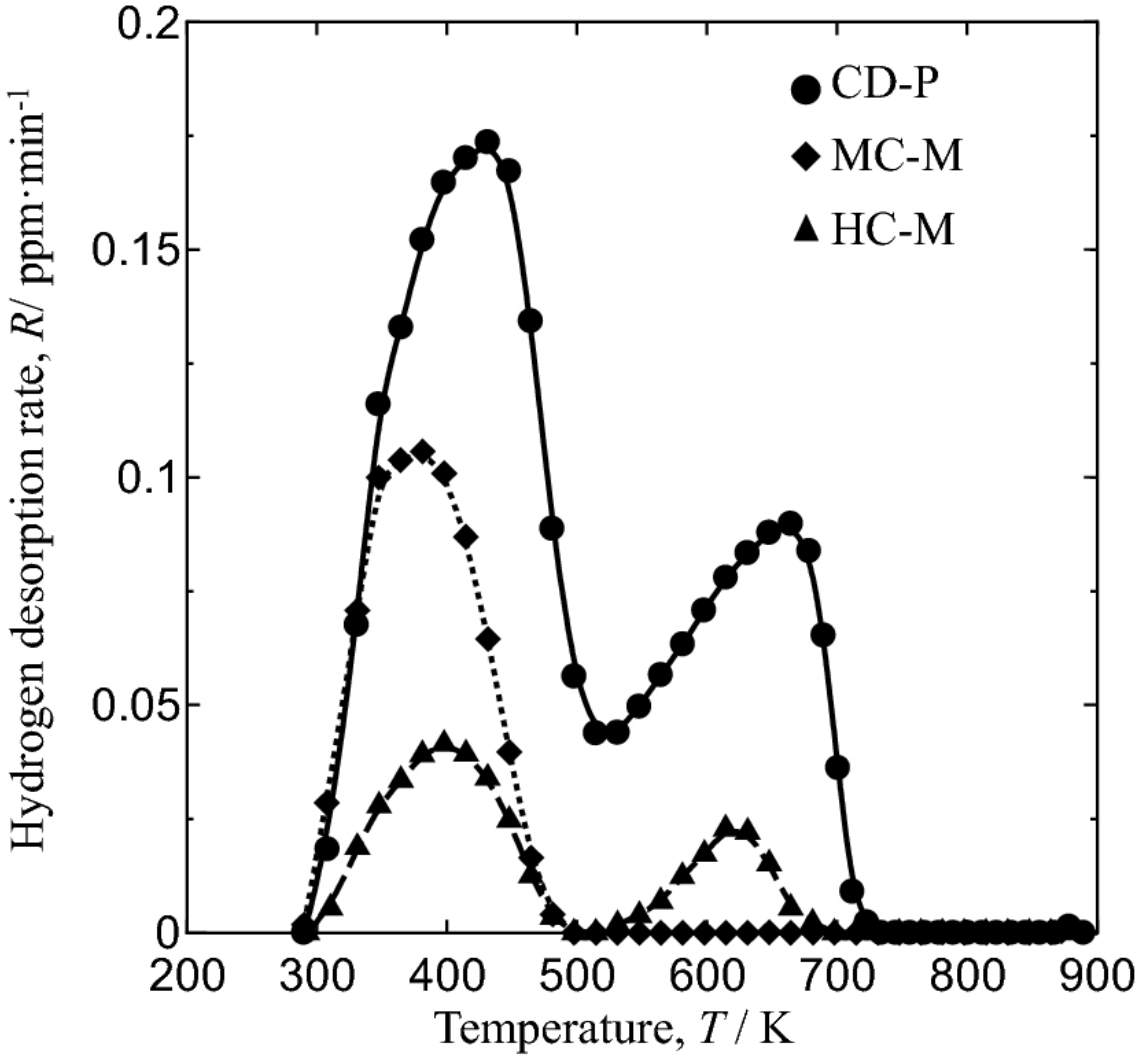

Figure 22 Thermal desorption profiled for hydrogen charged samples CD-P, MC-M, and HC-M. [38]

The temperatures effects on X90 pipeline steels were tested in hydrogen atmosphere and at different temperatures. Graph showing its fracture shrinkage, ductility, elongation, cross-sectional shrinkage, and temperature can be seen in Figure 23. The values for shrinkage ratio

of fracture area (Ψ) and ductility (δ) were obtained by comparing the in solution and air results. Based on the results, the ductility and shrinkage ratio of fracture area was at the lowest at 313K i.e. around 40°C and had the highest embrittlement at this temperature. The dip of ductility in the graph was from 293K to 323K (20°C to 50°C). [39]

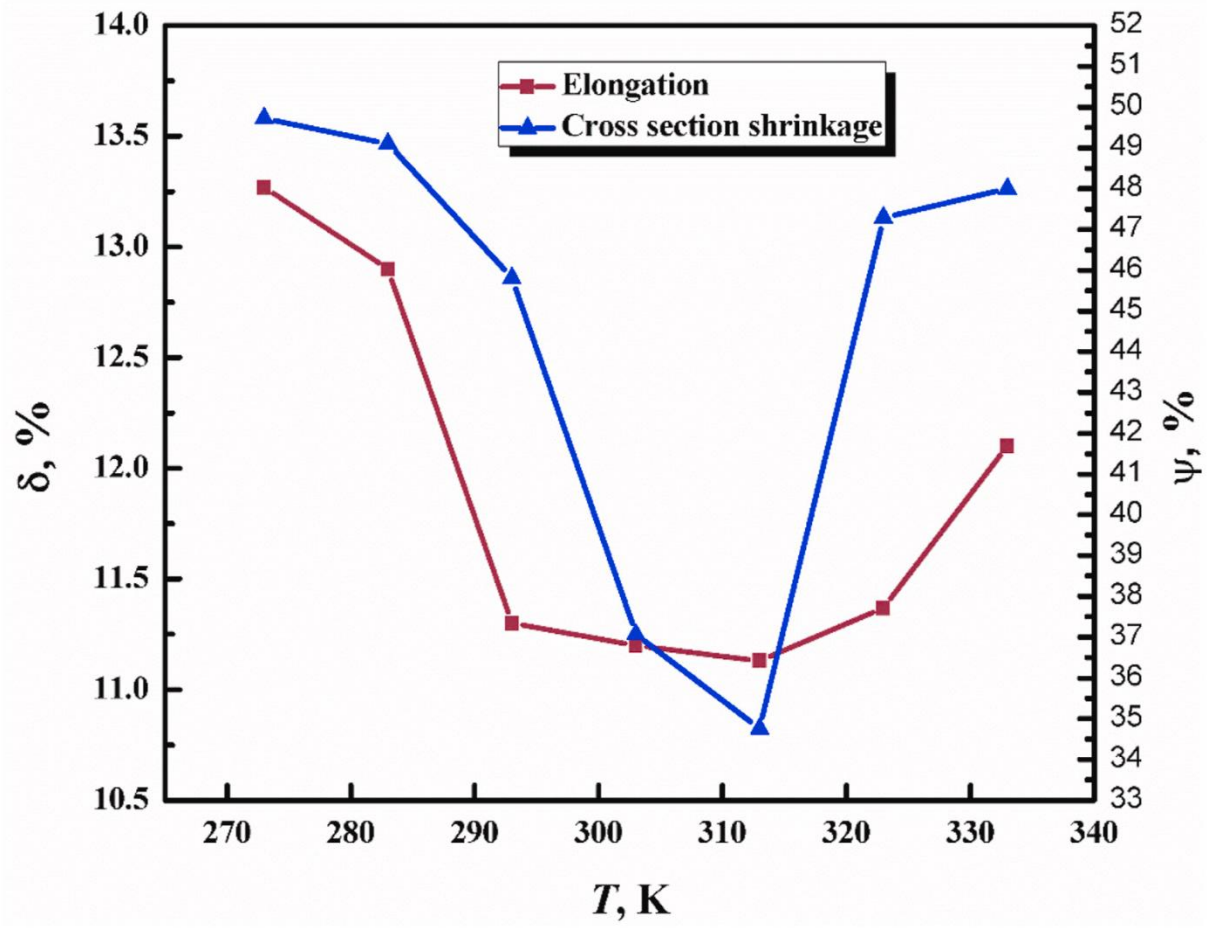

Figure 23 Ductility(δ) and fracture area shrinkage(Ψ) of X90 pipeline steel at different temperatures in NS4 solution. [39]

Higher hydrogen pressure has been shown to have a more negative effect on the material's mechanical properties. The most affected properties are the ductility, and the ultimate tensile strength.

Ultra-high strength martensitic steels were tested in different hydrogen gas pressures with slow strain rate testing (SSRT), and the martensitic steels had different prior austenitic grain sizes. The variation of the hydrogen gas pressure was from 0.21 to 5.5 MPa. Size of the prior austenitic grains were small (11.0µm), medium (12.9µm), and large (21.9µm). The graph showing the results is seen in Figure 24 and shows that the hydrogen pressure on all the samples lowered the beforementioned materials mechanical properties. [40]

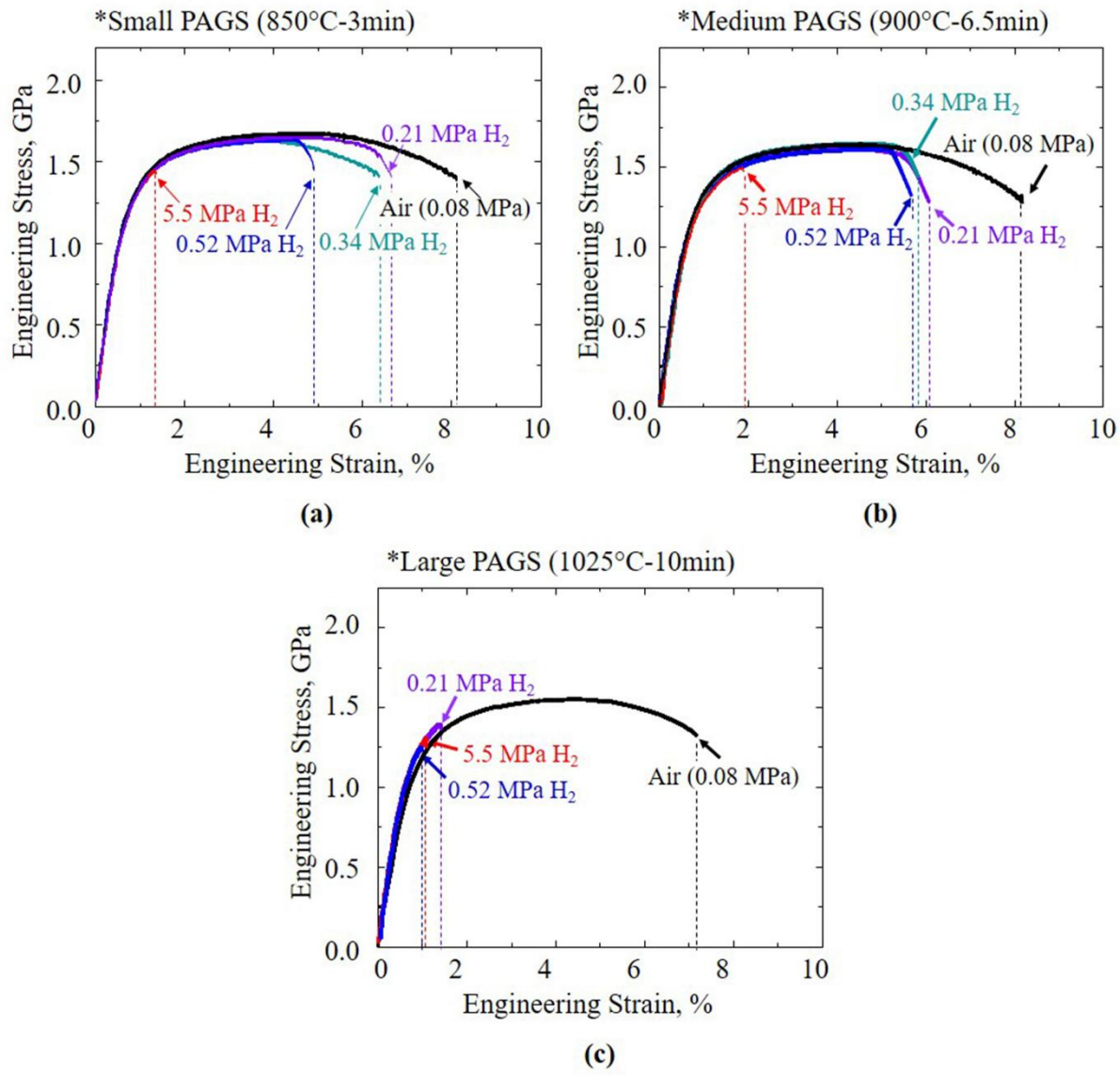

Figure 24 Engineering stress and strain curves for different doping pressures and prior austenitic grain sizes. [40]

Stainless steel 304 was tested in different partial pressures of hydrogen with SSRT. This was done by a gas that had 5% hydrogen and 95% argon. A graph for 5kPa and 3.5MPa partial pressures of hydrogen can be seen in Figure 25. With having 0.1 MPa and 70 MPa real pressure of the gas mixture. The stress strain curve indicates that the hydrogen gas pressure affected the stainless steel 304s' ultimate tensile strength, elongation, ductility, and toughness. [41]

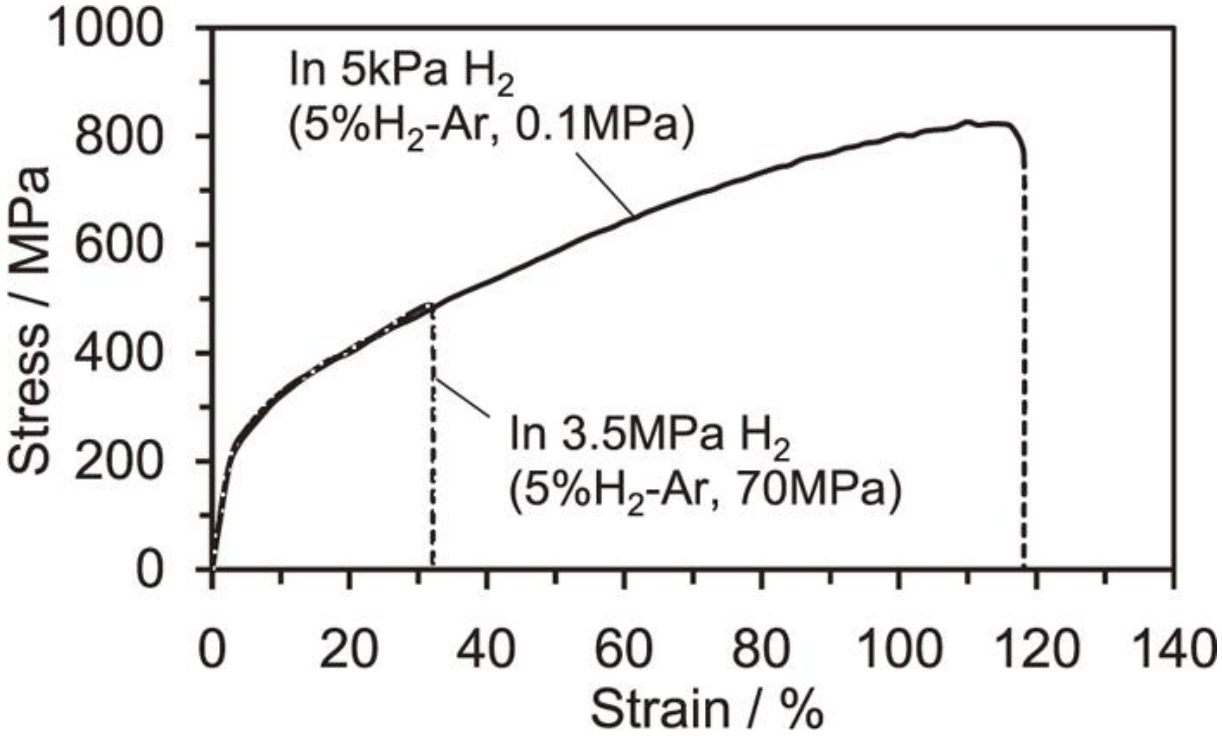

Figure 25 Stress strain curve of stainless steel 304 at different partial pressures of hydrogen. [41]

Exposure time to hydrogen can affect the materials' mechanical properties. As when the exposure time is high the materials defects and lattice get saturated with the hydrogen, i.e. the traps within the material get filled with hydrogen.

X52 steel was tested with 4.0 MPA hydrogen at different charging times and the engineering stress and strain curve can be seen in Figure 26. Showing that with higher charging times the strain gets lower i.e. the elongation decreases while ultimate tensile strength is similar to the original. [42]

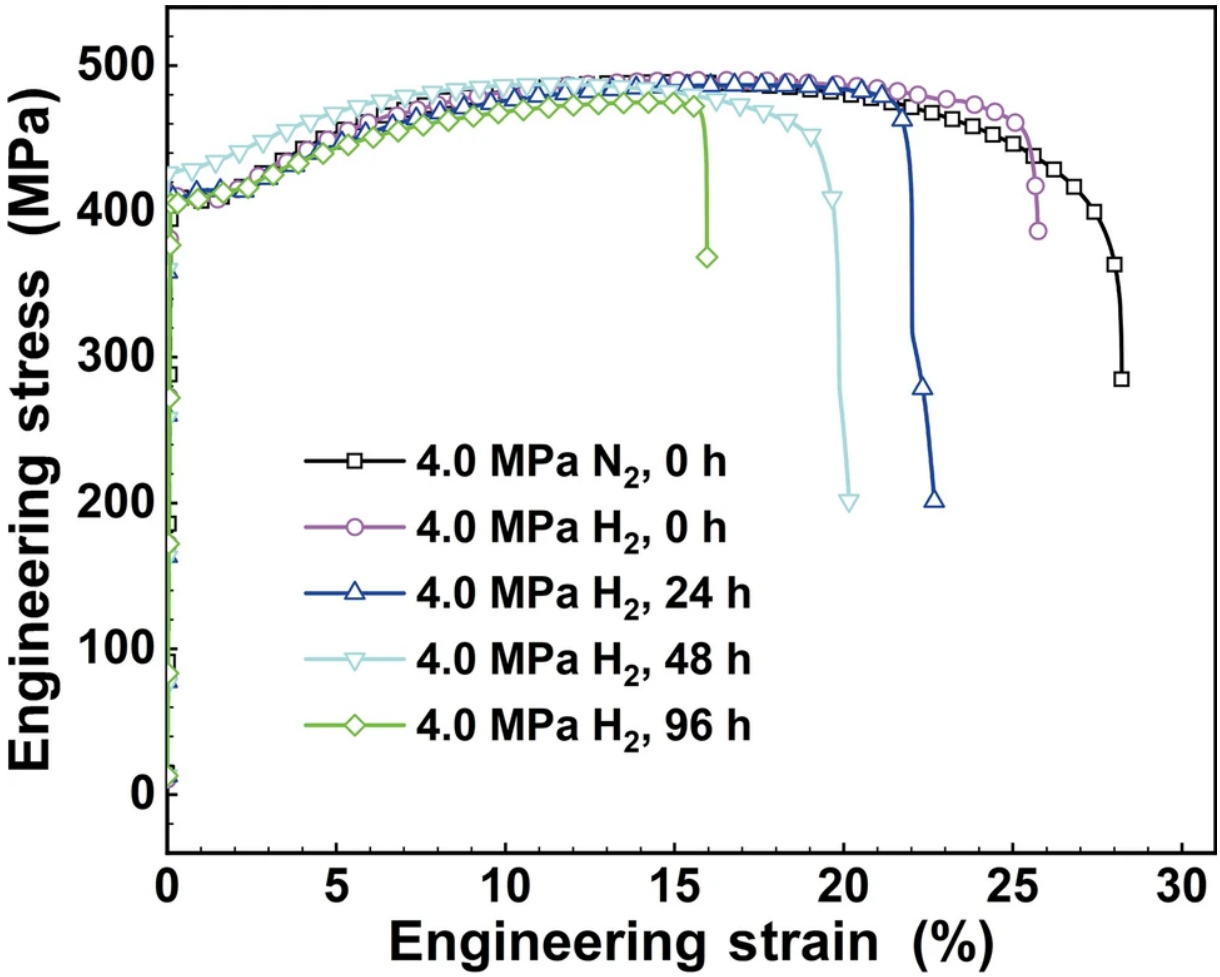

Figure 26 X52 engineering stress and strain curve with different charging times. [42]

2.5 Previous findings for the selected materials

The materials chosen for the thesis were 42CrMo4 quenched and tempered (QT), and X40CrSiMo 10-2. There has already been research on 42CrMo4, but none could be found for the X40CrSiMo 10-2.

In the study on 42CrMo4 different precharging methods were compared to each other. They tested the hydrogen content after each charging method. These charging's were done for notched tensile test samples with gaseous hydrogen at 19,5 MPa with temperature of 430°C and for 21 hours, and electrochemically for 3 hours with different electrolytes and current densities. For the gaseous hydrogen the hydrogen concentration was 1,2 parts per million (ppm), electrochemically with 1 M H_2SO_4 solution with 0,25 g/l of As_2O_3 and current density of 1 mA/cm^2 had 1,2 ppm, 1 M H_2SO_4 solution with 0,25 g/l of As_2O_3 0.5 mA/cm^2 had 0,95 ppm, and 1 M H_2SO_4 solution 1 mA/cm^2 had 0,5 ppm. The Vickers hardness for the material was measured at 223 HV30 and it was quenched and tempered at 700°C for two hours.

Tensile testing were done ex-situ with gaseous hydrogen and 1 M H_2SO_4 solution with As_2O_3 with current density of 1 mA/cm^2 on notched tensile specimens and showed minimal change in their mechanical properties, around 4 – 13% HEI%. The notched tensile strength (σ_N) in-situ hydrogen tests results can be seen in Table 3. In-situ tests on the notched tensile specimens had the biggest HEI values on lower displacement rates. [43]

Table 3 Notched tensile strength tests results on hydrogen atmosphere i.e. in-situ testing. [43]

H-charging conditions	Dis.Rate (mm/min)	Time (min)	σ_N (MPa)	HEI (%)	Embrittled depth (mm)
AR	0,4	12,0	1330,0	–	–
1 M H_2SO_4 + As_2O_3 i = 1 mA/cm2	0,4	11,0	1069,0	19,6	0,5
	0,1	38,0	931,0	30,0	0,9
1 M H_2SO_4 + As_2O_3 i = 0.5 mA/cm2	1,0	6,0	1155,0	13,2	0,3
	0,4	15,0	1129,0	15,1	0,4
	0,1	51,0	1094,0	17,7	0,8
	0,05	112,0	972,0	26,9	0,8
	0,02	198,0	1030,0	22,6	0,8
	0,01	266,0	882,0	33,7	0,8
1 M H_2SO_4 i = 1 mA/cm2	1,0	7,0	1173,0	11,8	0,3
	0,4	16,0	1131,0	14,9	0,3
	0,10	59,0	1124,0	15,5	0,6
	0,05	158,0	1115,0	16,2	0,7
	0,02	225,0	1134,0	14,7	0,4
	0,01	456,0	1124,0	15,5	0,6

Another study looked at the effect of the quenching and tempering (QT) on the hydrogen embrittlement of 42CrMo4. The tests were done in air and in-situ in two different electrolytes: low H 1 M H_2SO_4 solution with current density of 1 mA/cm^2, and 1 M H_2SO_4 with 0.25g/L of As_2O_3 solution with the current density of 1 mA/cm^2. The in-situ tests results can be seen in Table 4. Showing that for the lower tempering temperature and time, the hydrogen embrittlement is seen to be more severe based on the nominal stress. Also, the amount of hydrogen embrittlement seems to be related to the hardness of the 42CrMo4. [44]

Table 4 In-situ hydrogen tests at different mediums on 42CrMo4 with different quenching and tempering temperatures. [44]

Steel Grade	Hardness	Test Conditions	Displacement Rate (mm/min)	σNS (MPa)	HEI (σNS) (%)
QT600-3m	484 HV	air	0,4	2055	--
		low H	0,01	476	77
		high H	0,01	457	78
QT600-30m	332 HV	air	0,4	1870	--
		low H	0,01	930	50
		high H	0,01	792	58
QT600-2h	307 HV	air	0,4	1701	--
		low H	0,01	1299	31
		high H	0,01	891	48
QT600-24h	280 HV	air	0,4	1455	--
		low H	0,01	1306	10
		high H	0,01	1083	26
QT725-4h	206 HV	air	0,4	1053	--
		low H	0,01	961	9
		high H	0,01	851	19

In another study they quenched and tempered 42CrMo4 at different tempering temperatures. The hydrogen charging was done with gaseous hydrogen at 19,5 MPa and 450°C for 21 hours, after which the reactor was cooled down to 85°C. The tensile testing was done on smooth and notched tensile tests specimens. Smooth tensile tests showed minimal hydrogen embrittlement of the tested grades and their related Embrittlement indexes same as HEI% are seen in Figure 27. Showing that the highest amount of HEI% was around 12% for the grade tempered at 550°C and 6% for the one at 500°C. The results for notched tensile tests can be seen in Table 5. Showing that with the precharged samples the hydrogen content was higher in lower tempering temperature grades which also had a higher hardness. Also, the HEI% of the samples were higher in the lower tempering temperature samples. The fracture mechanism plasticity-related hydrogen induced cracking (PRHIC) is described to be “micro-plastic tearing on a very fine scale, along martensite lath interphases.” [45] The testing speed, i.e. the displacement/strain rate, also affected the amount of embrittlement, but with very low testing speed the hydrogen content in the sample lowered due to desorption as there was no hydrogen atmosphere while testing. [45]

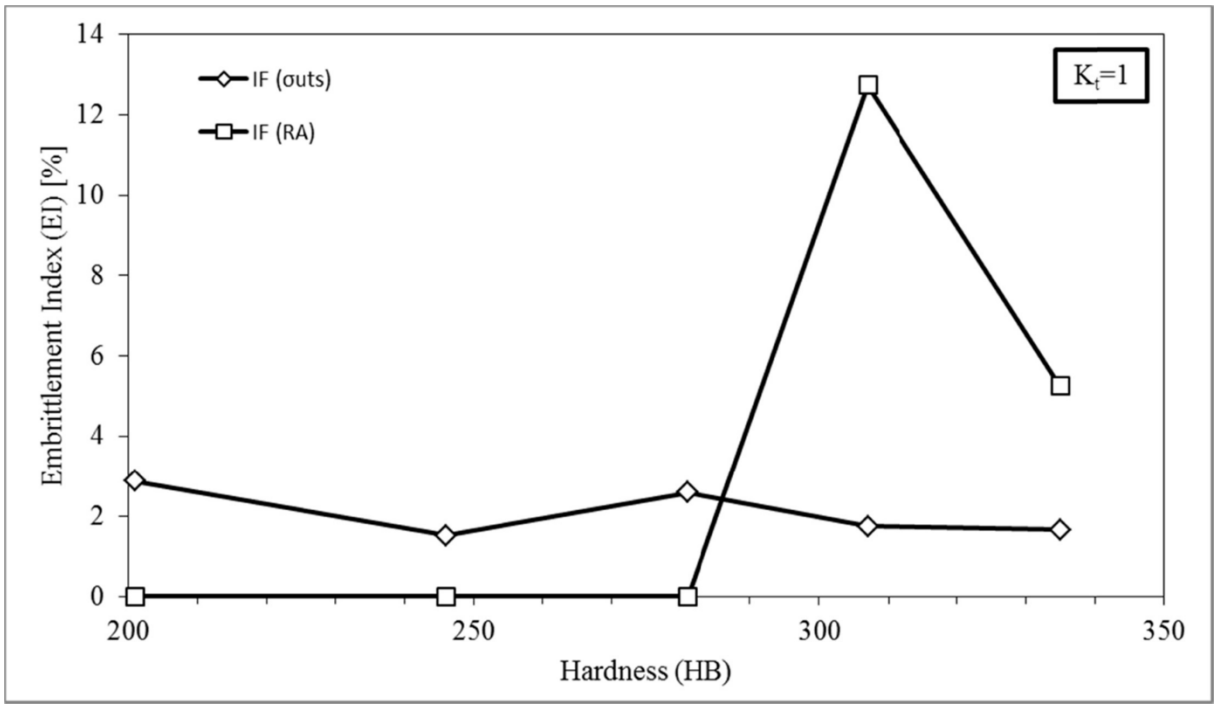

Figure 27 Different embrittlement indexes same as HEI for the different steel grades. [45]

Table 5 Test results of notched tensile tests for hydrogen precharged (ex-situ) samples. [45]

Steel Grade	Test speed [mm/min]	Test duration	CH [ppm]	σN [MPa]	RA [%]	HEI(σuts) [%]	HEI(RA) [%]	Fracture Micromechanisms
42CrMo4 700 (201HB)	0,4	12 min	Uncharged	1330	12,5	–	–	MVC
	0,4	9 min	1,2	1273	11,8	4	6	MVC
	0,04	80 min	1,2	1258	10,3	5	18	MVC
	0,004	14 h	1,2 → 0,7	1294	9,6	3	23	MVC
42CrMo4 650 (246HB)	0,4	17 min	Uncharged	1582	11,9	–	–	MVC
	0,4	15 min	1,2	1527	11,8	3	1	MVC
	0,04	105 min	1,2	1508	8,9	5	25	MVC+PRHIC
	0,004	16 h	1,2 → 0,85	1487	7,9	6	34	MVC+PRHIC
42CrMo4 600 (281HB)	0,4	12 min	Uncharged	1724	8,5	–	–	MVC
	0,4	12 min	1,4	1604	7,6	7	11	MVC
	0,04	85 min	1,4	1384	6,0	20	29	MVC+PRHIC
	0,004	14 h	1,4 → 1,0	1336	3,4	23	60	MVC+PRHIC+IG

42CrMo4 550 (307HB)	0,4	8 min	Uncharged	1800	7,5	–	–	MVC
	0,4	9 min	1,7	1602	6,3	11	16	MVC+PRHIC+IG
	0,04	65 min	1,7	1303	4,9	28	35	MVC+PRHIC+IG
	0,004	11 h	1,7 → 1,6	1248	2,7	31	64	MVC+PRHIC+IG
42CrMo4 500 (335HB)	0,4	15 min	Uncharged	1833	6,4	–	–	MVC
	0,4	13 min	1,9	1534	4,7	16	27	MVC+PRHIC+IG
	0,04	80 min	1,9	1050	3,1	43	51	MVC+PRHIC+IG
	0,004	6 h	1,9 → 1,8	771	0,5	58	92	MVC+PRHIC+IG
MVC: microvoid coalescence; PRHIC: plasticity-related hydrogen induced cracking; IG: intergranular.								

2.6 Mitigation possibilities

This chapter reviews studies on mitigating the effects of hydrogen embrittlement but does not consider their potential impact on the internal combustion engine (ICE) components operating conditions/variables, such as temperature, pressure, and friction. Some approaches use protective coatings which may interact or impact the beforementioned operating conditions/variables. Also, the possible flaking of the coatings is not considered.

In the article the effects of pure nickel and nickel-graphene coatings on quenching and partitioning (QP) steels substrate were studied related to hydrogen embrittlement. Hydrogen environment was made with 0,2 M H_2SO_4 with 2g/L of thiocarbamide i.e. thiourea and the charging time was 5 min with two different current densities. The QP steels were coated with electroplating. SSRT tests were done ex-situ, and the results can be seen in Figure 28 and show that the pure nickel coating reduced the HE by a small margin. The nickel-graphene coating the effects of the HE was reduced by a lot when comparing the same current density doping tests done on the substrate material QP (uncharged). The total elongation loss on the nickel-graphene coating in hydrogen atmosphere was around 8% when comparing it to the same atmosphere test on the substrate material which was around 80%, the difference is around tenfold. The nickel-graphene coating seemed to have an effect on the diffusion of hydrogen to the substrate QP. [46]

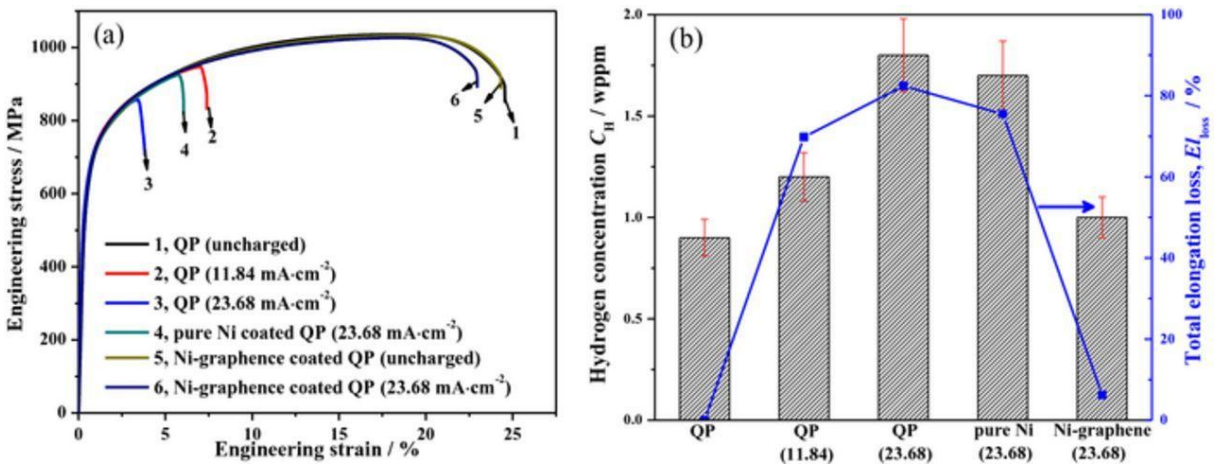

Figure 28 a) Stress and strain curve of different sample with and without coating, b) Their hydrogen concentration, and elongation loss. [46]

In the study copper samples coated with graphene. Hydrogen charging was done with 0,5M H_2SO_4 with 250 mg/L of As_2O_3. SSRT test results are shown in Figure 29 and the difference between the charged pure copper and graphene coated was around 8%. The difference between the uncharged pure copper and charged with graphene coated was around 3%. The hydrogen embrittlement ratio (HER) between charged pure copper and graphene coated were 10% and 3% respectively. [47]

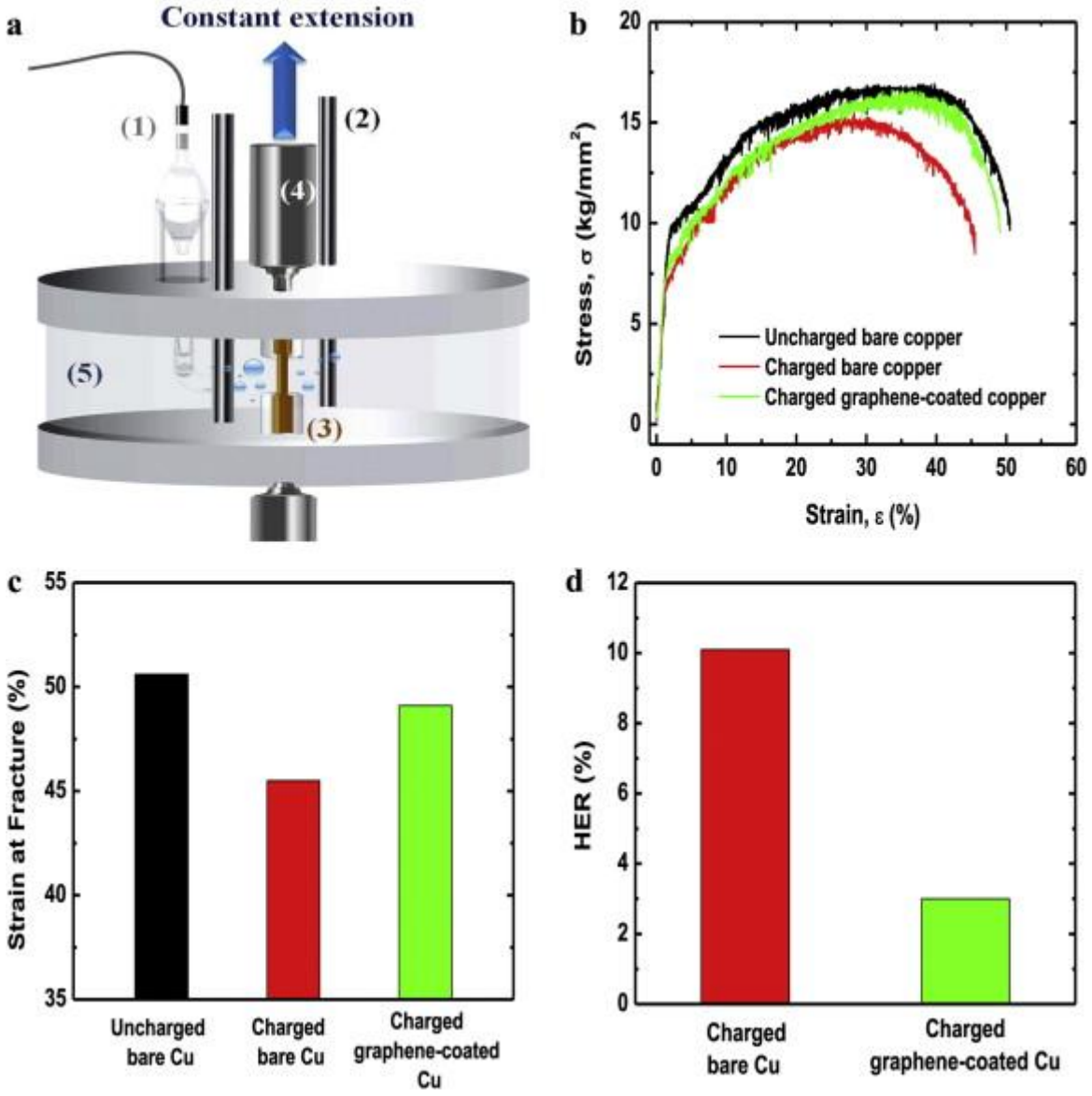

Figure 29 SSRT test schematic and the results from the tests of pure copper and graphene coated pure copper. [47]

3 Methodology

3.1 Testing setup

The testing setup was decided based on previous studies of the material 42CrMo4 and the available equipment. The hydrogen charging will be done with electrochemical charging. This will be done ex-situ i.e. the samples will be precharged before the tensile testing. The type of tensile testing samples will be notched tensile testing samples. The dimensions of these samples will have similar dimensions between the shoulders and have a different grip section as in the previous studies ([43], [44], [45], [48]). The exact same dimension could not be machined. The dimensions of the machined samples are seen in Figure 30. Four samples will be made from 42CrMo4 QT and X40CrSiMo10-2. One sample from each will be tested in air and the other with hydrogen precharging. The charging is done in an acidic electrolyte of 1 M H_2SO_4 and 2 g/l of thiourea, with a current density of 1 mA/cm^2 for 6 hours. Thiourea is added to block the recombination of hydrogen. In the study ([43]) the saturation time of the 42CrMo4 was tested and the result was that at around 3 hours the samples became saturated. The selection of 6 hours for the charging is due to not having any data on the saturation time of the X40CrSiMo 10-2. The tensile testing will be done for both non-charged and charged samples with a displacement rate of 0,1 mm/min. The machining, hydrogen charging, and tensile testing were done by the University of Oulu based on the variables above.

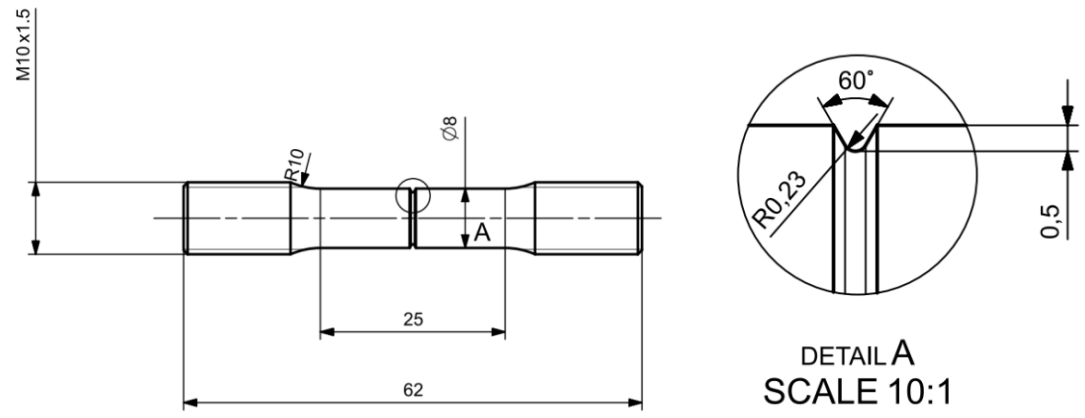

Figure 30 Dimensions of the notched tensile test specimens.

3.2 Equipment used for experiments

Equipment	Picture of equipment	What was it used for
MEBA MEBASWING 320 G-HSS		Component cutting to fit them in the abrasive cutter
Buehler Delta Automatic Abrasive Cutter		Cutting components to the size needed for tensile specimen milling

Struers Labopress-3		Sample pressing for the grinding and polishing machine, and for metallographic samples
Struers Tegramin-30 grinding and polishing machine		Grinding and polishing to obtain wanted surface finish on samples

Leica DM6 M		Optical microscope for microstructure analysis
Struers Duramin-40 hardness measurer		Hardness measurements

Wolpert hardness measurer		Hardness measurements
Hitachi FOUNDRY-MASTER smart, spark Optical Emission Spectroscopy (OES)		Chemical composition measurement

TESCAN VEGA3 and Thermo Scientific EDS-detector		High resolution Scanning Electron Microscope (SEM) images and chemical composition measurements with Energy Dispersive Spectroscopy (EDS)
Hydrogen charging cell with 1M H2SO4 + (2 g/l) thiourea and a MMO (mixed metal oxide) mesh electrode (University of Oulu)	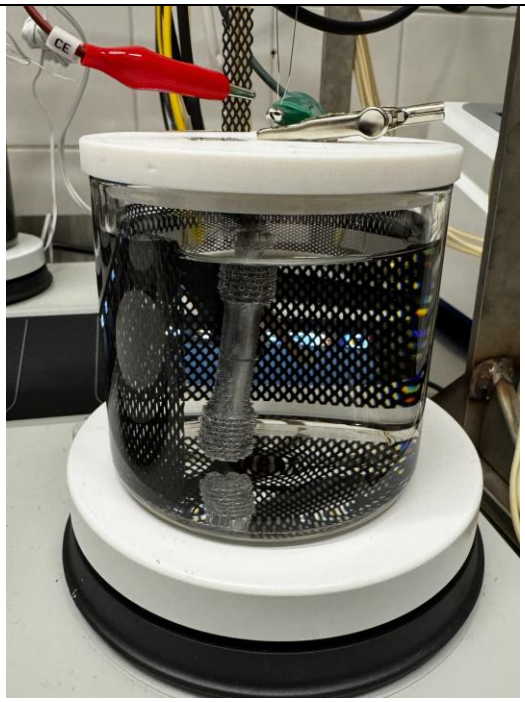	Hydrogen cell for doping of the samples

Zwick 100kN Tensile testing machine (University of Oulu)		Tensile testing of the non-charged and hydrogen charged samples

3.3 Testing procedure made by University of Oulu

1) Machining the specimens to threaded round notched tensile bars

    1. X40CrSiMo 10-2 hydrogen sample was made from sample 1 in Table 7 and the non-charged one from sample 2. (Table is seen in Chapter 4.2 Microstructure analysis)

2) H-charging surface preparation = polishing the between-the-threads area with 1200 grid sandpaper

3) Spot-welding a wire for coupling the specimen to a working electrode

4) H-charging the specimens at room temperature

    1. In electrolyte of 1M H_2SO_4 and 2 g/l of thiourea, with a current density of 1 mA/cm^2 for 6 hours

5) Transfer of the specimen from the H-charging to the tensile testing. There was 3-minute downtime from the end of hydrogen charging to the tensile tests start.

6) Tensile testing of the specimens

7) After the hydrogen charged tensile tests, the fracture surfaces were rinsed again with ethanol to suppress possible rusting

8) Exporting the data + template report

3.4 Analysis methods

The material will be tested before any tests to see if they fit the standard for the chemical composition and the hardness will be checked to see how the results fit the previous studies. The chemical composition will be measured with spark Optical Emission Spectroscopy (OES) and the hardnesses with Vickers and Brinell hardness measurers.

With spark OES the sample is burned with an electrode in an argon atmosphere. The machine then analyses the visible range of light and its intensity at different wavelengths with detectors. These certain wavelengths have been specified to a certain basic element and with software the intensities are then converted to a mass percentages, and that is how you obtain the chemical composition of the sample. [49]

Vickers and Brinell hardnesses are measured by indenting the sample with a pyramid shaped and a ball shaped indenter respectively. In ideal conditions the Vickers hardness measurements pyramid indenter makes a square indentation on the sample. The squares dimensions from each sharp end to the opposite one are measured and are used to obtain value of d1 and d2. The equation for surface of the indentation (d) in equation (5) is the same in both measurement methods but the d1 and d2 measurement methods are different. The Vickers hardness of the material can then be calculated based on the equation (6) in which the test load is F. The Brinell hardness indentation is made with a ball which leaves a circle indentation on the sample from which the ball's diameter is measured from two different locations with 90° in between the measurements. These values are then used to obtain the surface of the indentation (d). The Brinell hardness is then calculated with the equation (7). Usually, modern hardness measurers use automatic calculations to obtain the hardnesses or from a list of precalculated hardness values for a specific surface of the indentation (d). [50]

$$d = \frac{d1+d2}{2} \tag{5}$$

$$HV \approx 1{,}854 \times \frac{F}{\left(\frac{d1+d2}{2}\right)^2} \tag{6}$$

$$HB = 0{,}102 \times \frac{2F}{\pi D^2 \left(1-\sqrt{1-\frac{d^2}{D^2}}\right)} \tag{7}$$

The tensile testing data will be analyzed and made into a stress strain curve. The HEI% will be calculated based on the notched fracture strength, ultimate strength, and strain data gathered by the tensile testing. The HEI% i.e. reduction will also be calculated based on the

toughness. In equation 8 the formula for calculating the overall toughness for the material is seen. The method is called trapezoidal rule which approximates the area under the curve based on the small trapezoids made between each measurement point in the tensile testing data. The fracture type can be estimated based on the stress strain graph and the other data, but it can be verified with Scanning Electron Microscope (SEM) high magnification images.

$$Toughness = \sum_{i=0}^{n-1} \frac{(\sigma_i + \sigma_{i+1})}{2} (\varepsilon_{i+1} - \varepsilon_i) \quad (8)$$

The fracture type will be checked with SEM, and the length of the embrittlement depth will be measured. SEM works by blasting electrons from a filament of the electron gun. These electrons are then aligned with an anode, magnetic lenses and stigmators, to have the electrons in the wanted way as these affect the image quality of the SEM. After the electrons have hit the wanted surface i.e. the sample some of them scatter back by only losing small amount of energy and others are from close to the surface with lower energy. The higher energy electrons that have scattered back are called backscattered electrons (BSE) and they can show more about the material as they are from slightly below the surface. In BSE images, the higher the Z-value of the element is, the brighter the gray scale. For example, if there is iron (Fe) with Z-value of 36 and oxygen (O) with 8 the areas with oxygen are darker compared to the iron ones. The electrons from near the surface with lower energy are called secondary electrons (SE) and they show more about the topology of the sample which is more used in analysis of fracture surfaces. The BSE image can also tell about differences in depth and thus both SE and BSE are used simultaneously while analyzing. [51]

4 Results and Discussion

This chapter will look at the experimental parts test and results. These will be then discussed in the subchapters. Possible future developments ideas will be discussed in their own subchapter.

4.1 Chemical composition analysis

The chemical composition for the component's materials were checked with Hitachi's OES. The material X40CrSiMo 10-2 chemical composition was measured from two samples as the tensile testing samples will be made from two different components. The material 42CrMo4 chemical composition was measured from only one sample as the tensile testing samples were made from one component and from the same area. The results for the chemical composition measurements for 42CrMo4 are shown in Table 6, and for X40CrSiMo 10-2 in Table 7. For X40CrSiMo 10-2 the tensile test samples chemical compositions are closely matched together thus the difference should not affect the hydrogen tests.

Table 6 42CrMo4 chemical composition standard and test result from the sample.

42CrMo4	C	Cr	Mn	Mo	P	S	Si
Sample	0,490	1,000	0,684	0,215	0,010	0,008	0,245

Table 7 X40CrSiMo 10-2 chemical composition standard and test results from the samples.

X40CrSiMo 10-2	C	Cr	Mn	Mo	Ni	P	S	Si
Sample 1	0,411	8,920	0,437	0,035	0,086	0,018	0,006	2,650
Sample 2	0,413	9,010	0,440	0,036	0,085	0,016	0,007	2,630

4.2 Microstructure analysis

The same samples were then mounted in a resin and grinded and polished for etching. The 42CrMO4 and the X40CrSiMo 10-2 samples were etched with Vilella's etchant that was made from 100ml of ethanol, 5ml of HCl, and 1 gram of picric acid. The microstructure images obtained with the Leica Dm6 M with different magnifications can be seen in Figure 31 - Figure 34. They show that the microstructure of the sample's material was martensitic type. On the 42CrMo4 the martensitic laths are seen better. In X40CrSimo 10-2 the martensitic type of structure could be identified with low magnification and contained a lot of carbides. The number of carbides was similar in both the samples 1 and 2. The type of carbides on samples of X40CrSiMo 10-2 were checked with SEM/EDS. The measurement points can be

seen in Figure 35 and Figure 36, and the corresponding chemical composition results in Table 8 and Table 9. They showed that the carbides are chromium (Cr) carbides as the level of it was high compared to the base materials level. So, based on the measurements and comparison of the two different materials, the hypothesis for the tensile tests is that the X40CrSiMo 10-2 will be more prone to hydrogen embrittlement. As, the Cr-carbides are one type of irreversible hydrogen trap, and it has more of them.

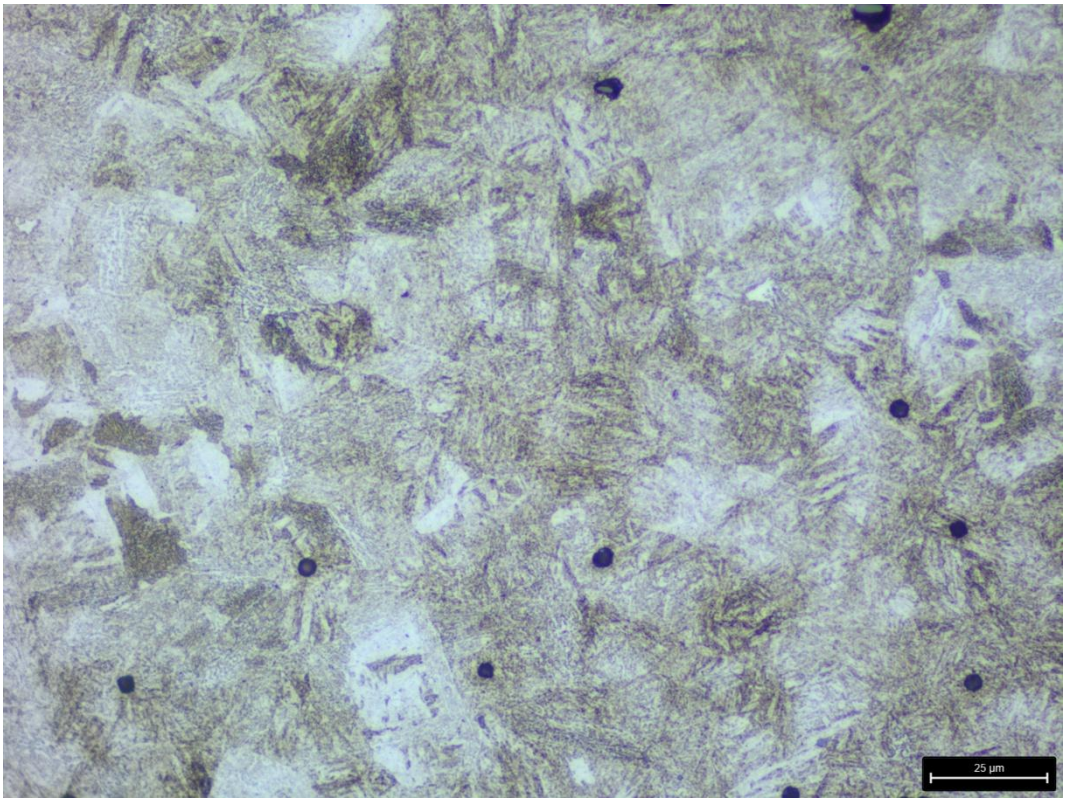

Figure 31 Microstructure of 42CrMo4 etched with Vilella on 500x magnification.

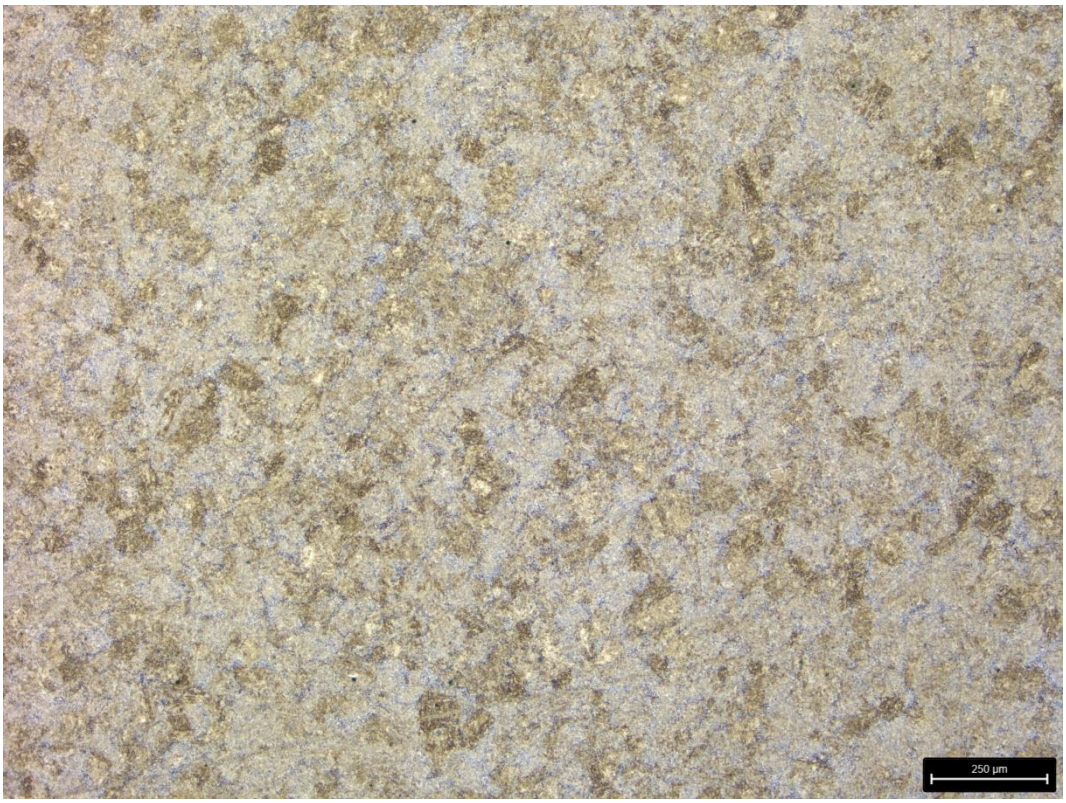

Figure 32 Microstructure of X40CrSiMo 10-2 sample 1 etched with Vilella on 50x magnification.

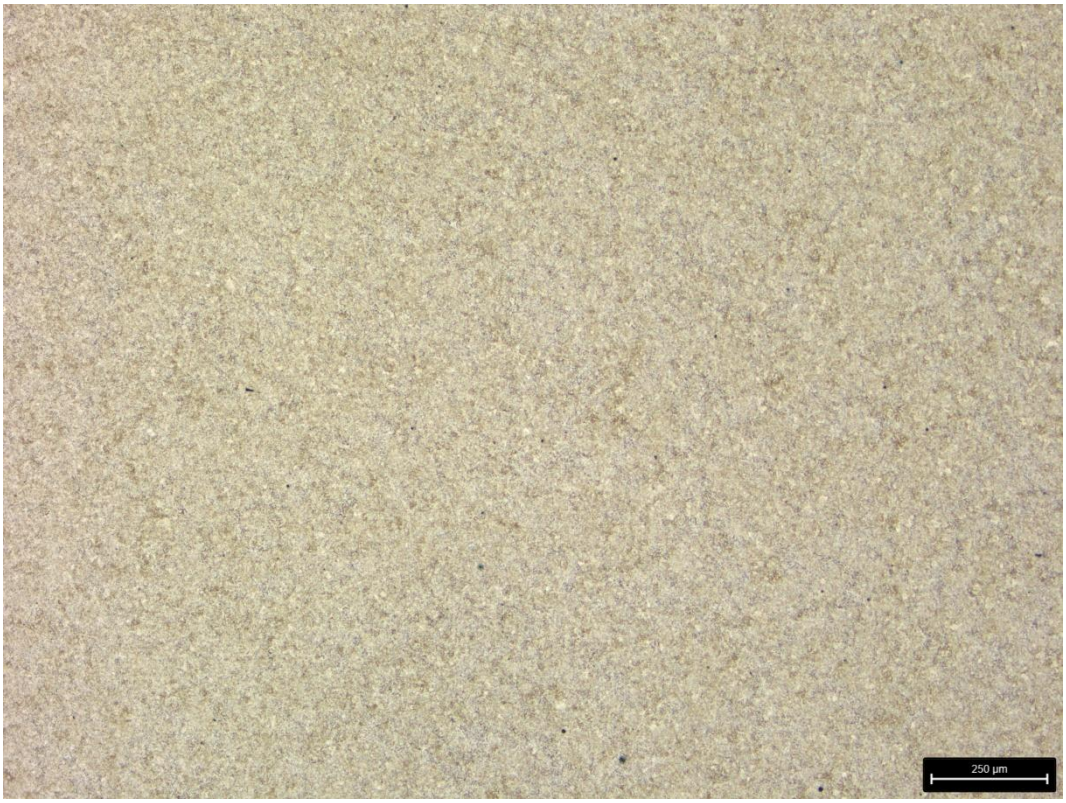

Figure 33 Microstructure of X40CrSiMo 10-2 sample 2 etched with Vilella on 50x magnification.

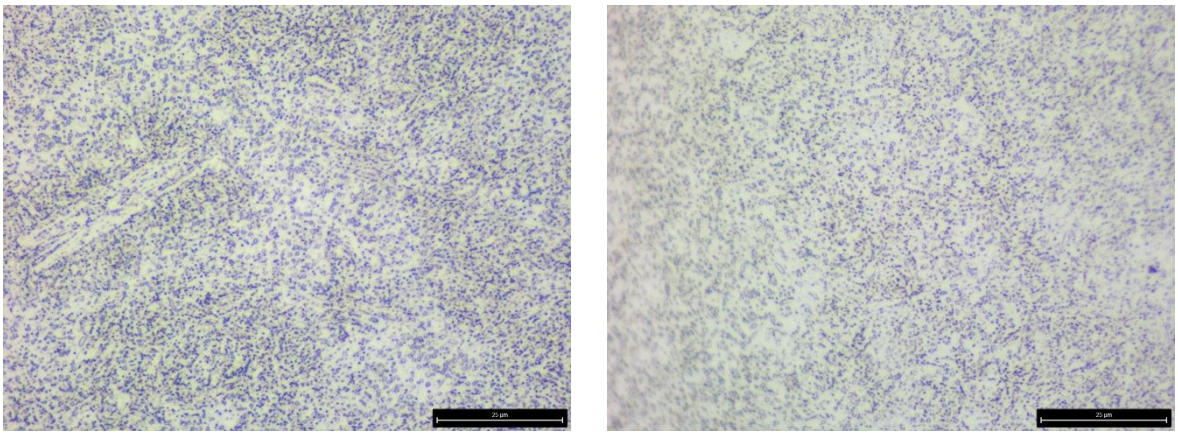

Figure 34 X40CrSiMo 10-2 microstructure of both sample 1 (left) and sample 2 (right) were taken with 1000x magnification.

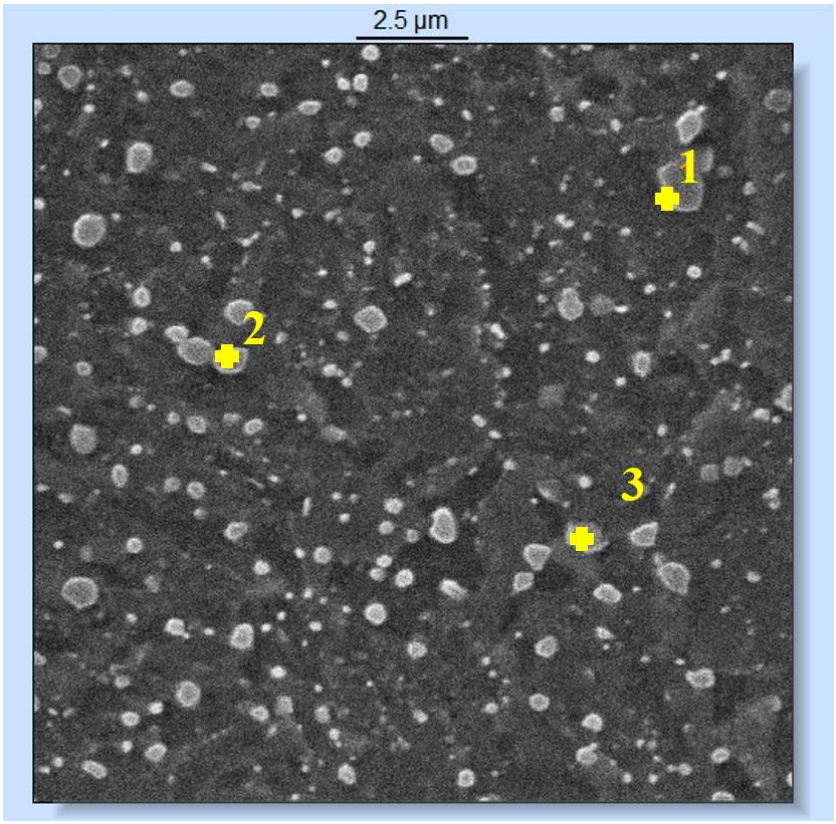

Figure 35 EDS measurement points for sample 1 of X40CrSiMo 10-2.

Table 8 Results of the EDS measurements of X40CrSiMo 10-2 sample 1.

	C	Si	Cr	Mn	V	Fe
X40-1 base material	-	2.83	9.60	-	-	87.58
X40-1 point 1	1.32	1.58	28.97	1.40	-	66.73
X40-1 point 2	1.10	2.14	20.10	-	-	76.67
X40-1 point 3	1.08	1.62	31.75	-	0.77	64.78

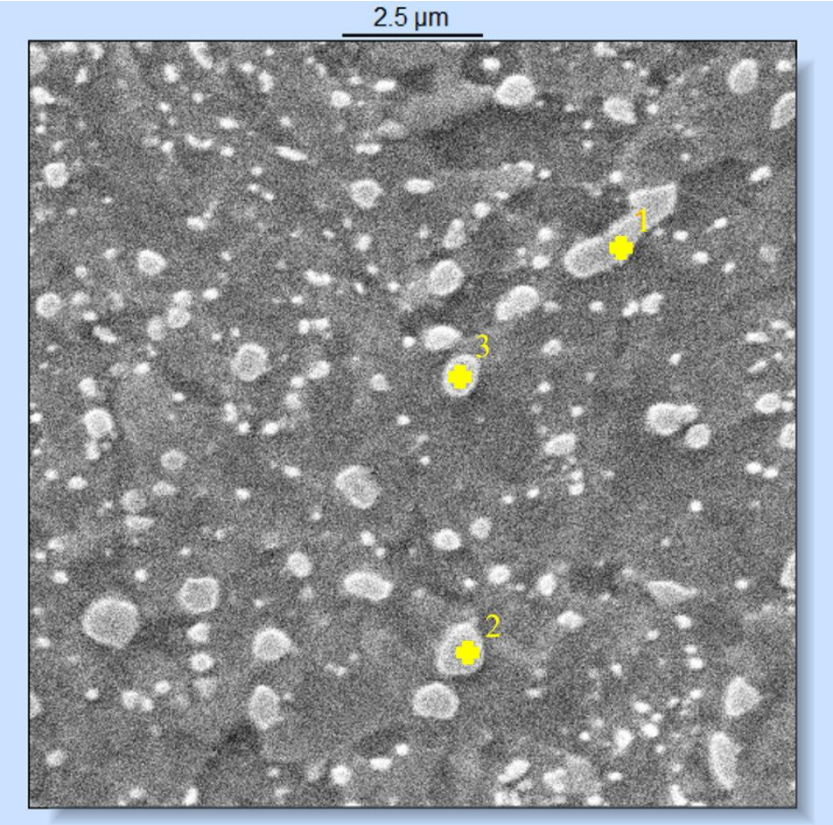

Figure 36 EDS measurement points for sample 2 of X40CrSiMo 10-2.

Table 9 Results of the EDS measurements of X40CrSiMo 10-2 sample 2.

	C	Si	Cr	Fe
X40-2 base material	-	2.79	10.26	86.95
X40-2 point 1	1.21	2.21	26.44	70.14
X40-2 point 2	1.08	2.46	22.91	73.55
X40-2 point 3	1.35	2.32	28.07	68.26

4.3 Hardness tests

The hardness of the material was tested with the Struers Duramin-40 and Wolpert hardness measurers. The tests for the hardness on Duramin-40 were done with Vickers hardness measurement head and with a force of 10 kg. The measurement grid was 3x3 cm. With Wolpert the measurements were done with Brinell hardness measurement head, and the ball diameter was 2.5 mm and the force 187.5 kg. Five different spots were measured. The averages of the hardness tests can be seen in Table 10.

Table 10 Hardness measurement test results averages.

Hardness tests	42CrMo4	X40CrSiMo 10-2 sample 1	X40CrSiMo 10-2 sample 2
HV10	282,9	295,5	291,3
HB	285,2	291,8	287,8

4.4 Tensile testing results

The tensile tests were all conducted at room temperature ~21°C. The stress strain graphs for each material with and without hydrogen charging can be seen in figures (Figure 37 - Figure 40) and combined into one in Figure 41. The mechanical properties from these graphs can be seen in Table 11. Based on the mechanical properties the HEI% were calculated and are shown in Table 12. The results show that both materials were prone to hydrogen embrittlement. Based on the calculated HEI% the X40CrSiMo 10-2 was more prone to it. As, the reduction of both toughness and strain were 67,7% and 60% respectively. While on 42CrMo4 the values were 54,9% and 52,1% respectively. The fracture point's strength HEI% for X40CrSiMo 10-2 lower by 6,7% and for the 42CrMo4 it was higher by 10,3%. The HEI% calculated by the ultimate tensile strength showed that for the X40CrSiMo 10-2 value was lowered by 6,7% and for 42CrMo4 by 3,3%. These findings show that the mechanical properties were mostly lowered by the reduction in strain. Thus, it also impacts the toughness of the material. The amount of reduction in the toughness could affect the components lifetime. As, the material cannot absorb the same amount of energy as the original component material. There only being one test per condition could affect the tests results as there could be anomalies.

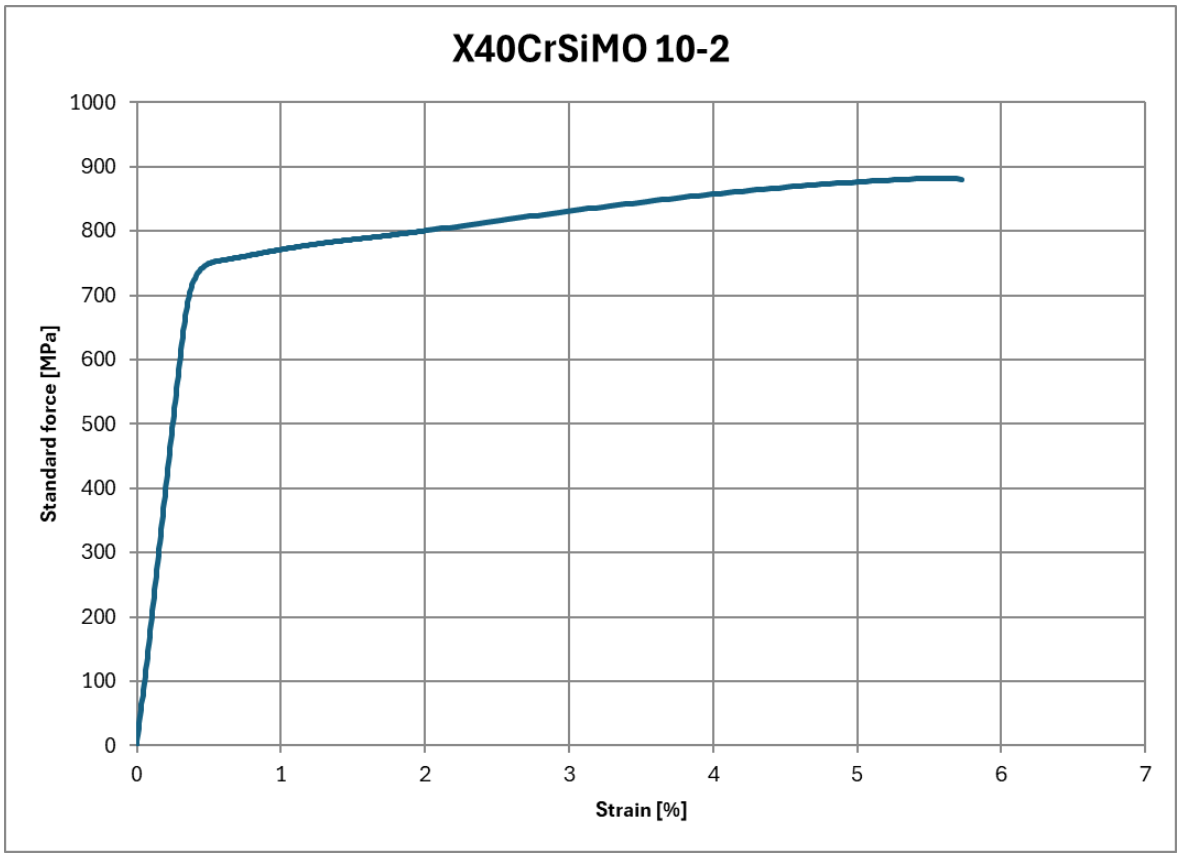

Figure 37 Stress strain graph of non-hydrogen charged X40CrSiMo 10-2.

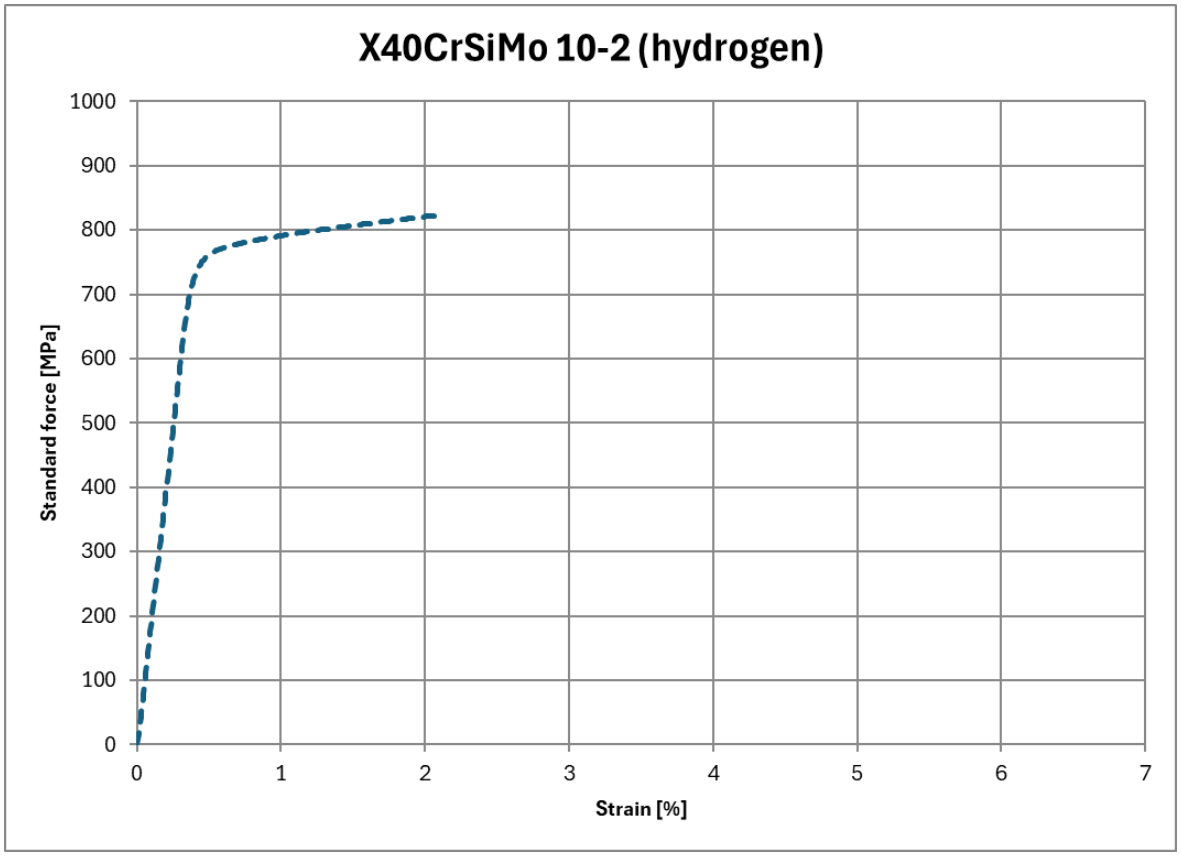

Figure 38 Stress strain graph of hydrogen charged X40CrSiMo 10-2.

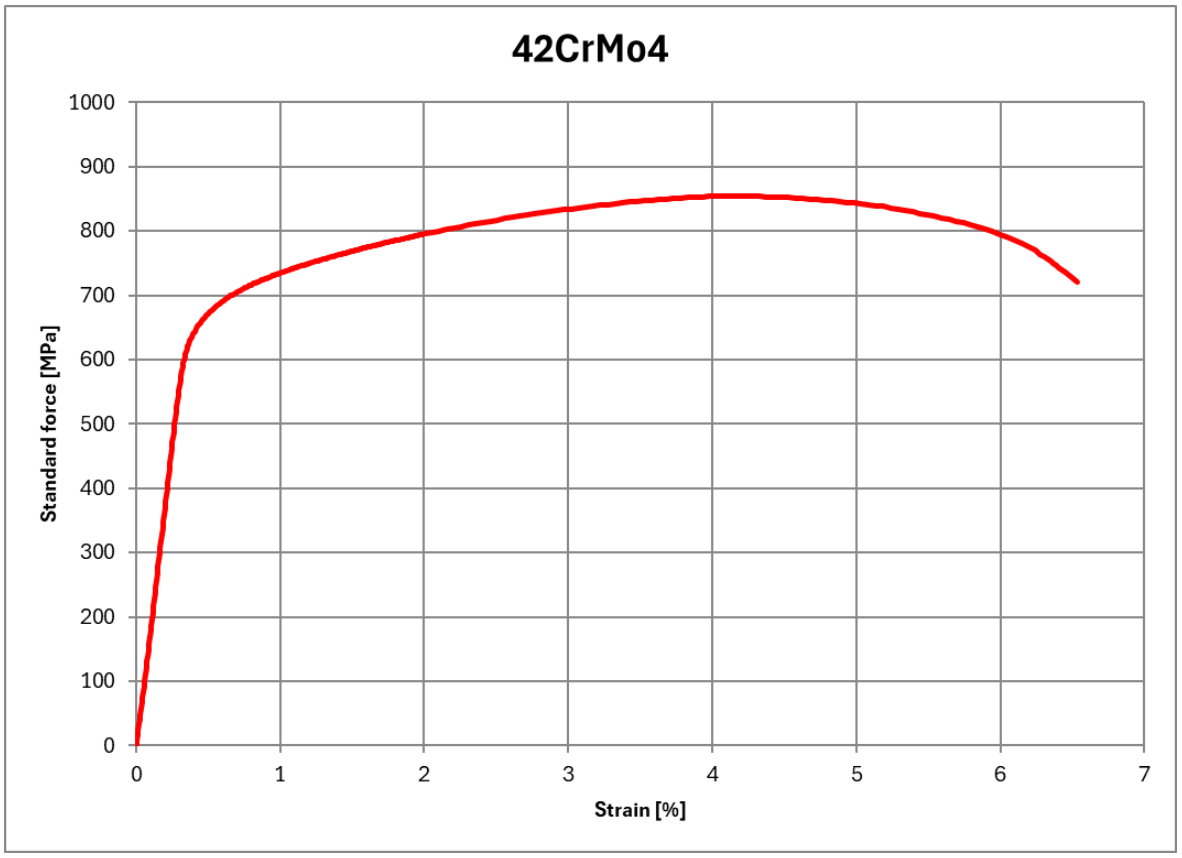

Figure 39 Stress strain graph of non-hydrogen charged 42CrMo4.

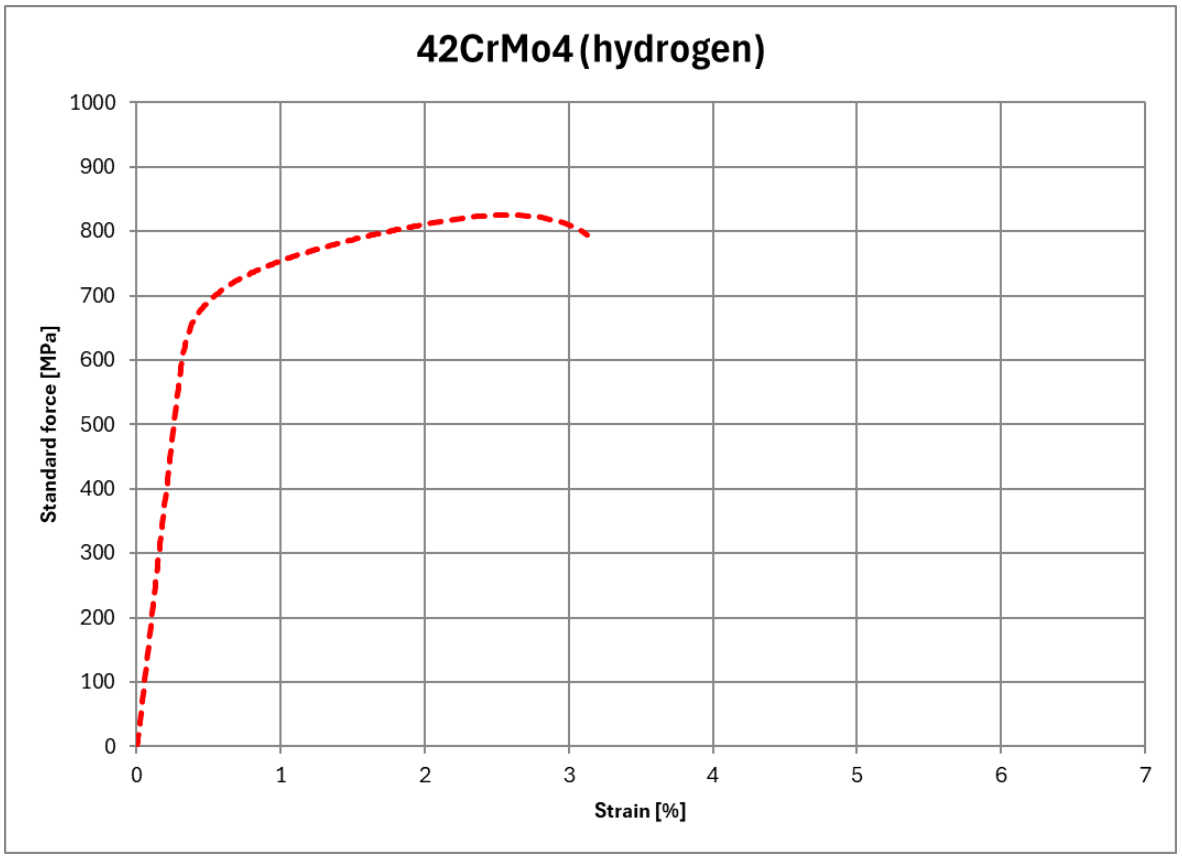

Figure 40 Stress strain graph of hydrogen charged 42CrMo4.

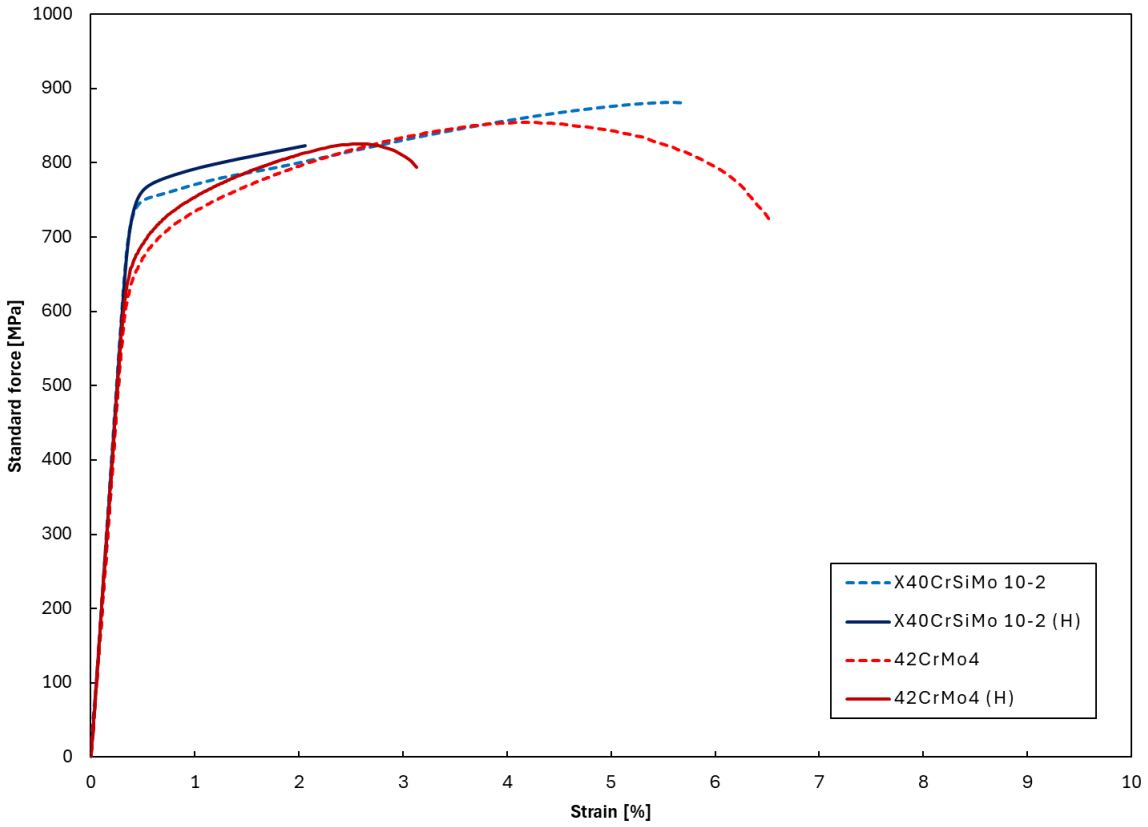

Figure 41 Stress strain graph showing all the tested samples in one graph.

Table 11 Tensile test results for all the samples, ones with (H) are the hydrogen charged ones.

Specimen identifier	m_E	$R_{p0.2}$	R_m	$A_{t\ (corr.)}$	Toughness	t_{Test}
Unit	GPa	MPa	MPa	%	MJ/m³	s
X40CrSiMo 10-2	206,38	753,94	881,95	5,17	4566,30	13,87
X40CrSiMo 10-2 (H)	201,55	771,48	822,69	2,05	1475,50	6,28
42crmo4	195,82	684,02	854,34	6,52	5075,39	16,63
42crmo4 (H)	204,48	701,44	825,87	3,12	2289,50	7,37

Table 12 Calculated HEI% for the ICE component materials.

HEI%	Fracture point strength	Ultimate tensile strength (Rm)	Strain (At (corr.))	Toughness
X40CrSiMo 10-2	6,72	6,72	60,17	67,69
42crmo4	-10,28	3,33	52,14	54,89

4.4.1 Tensile test result comparison to literature

The tensile testing results for 42CrMo4 differ from the ones found in literature for similar hardness values. Most comparable results from the literature are the ones found in Table 5, as they were also notched tensile tests with ex-situ hydrogen precharging. Closest displacement rate to the one chosen for experiments is 0,04 mm/min, the one used for experiments were 0,1

mm/min. The closest hardness is 281 HB, and the hardness tests showed that the tested material hardness was 285,2 HB. Also, the tests in air for both the literature results and the experimental samples results show that the materials had a high difference of ultimate tensile strength. With these given values the results for the literatures tests were that the HEI% based on ultimate tensile strength was 20% and based of reduction in area was 29%. They differ from the experimental parts increase based on the ultimate tensile strength of 10,3% and the reduction based on the strain of 52,1%. Both reduction in area and strain measure the ductility of the material. Thus, it can be said that the experiments' samples had higher loss of ductility than the ones found in literature.

4.5 Fracture surface analysis

The fracture surfaces were examined with SEM. The embrittlement depth could not be determined from the samples. This was due to the fracture type was not consistent near the edges.

Overview of the no-charged and hydrogen charged X40CrSiMo 10-2 fracture surfaces can be seen in Figure 42 and Figure 43 respectively. All the SEM images contain the secondary electron (SE) image on the left and backscattered electron (BSE) image on the right. The hydrogen charged samples fracture surface appears to be blockier compared to the non-charged one. This blocky like structure is looked at closer in Figure 44 and Figure 45. They show that the fracture type on the hydrogen charged one has flat areas typical for intergranular fractures, indicating of brittle fracture type. Some quasi-cleavage fracture could also be seen in Figure 44. The fracture surface on the non-charged sample also showed small signs of intergranular fracture type seen in Figure 46, which seems to be typical for the material. The hydrogen dope sample contained a bigger area of intergranular fracture type. Also, the intergranular fractures appeared to be more severe.

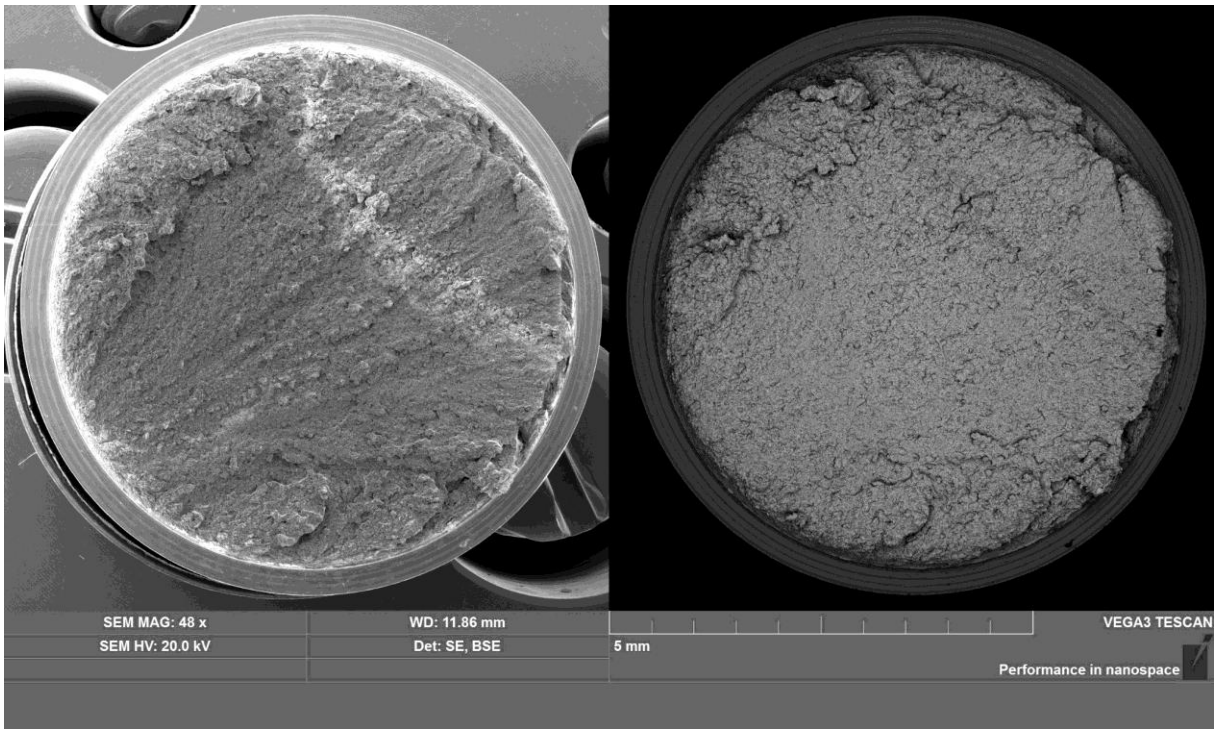

Figure 42 X40CrSiMo 10-2 non-hydrogen charged samples fracture surface overview.

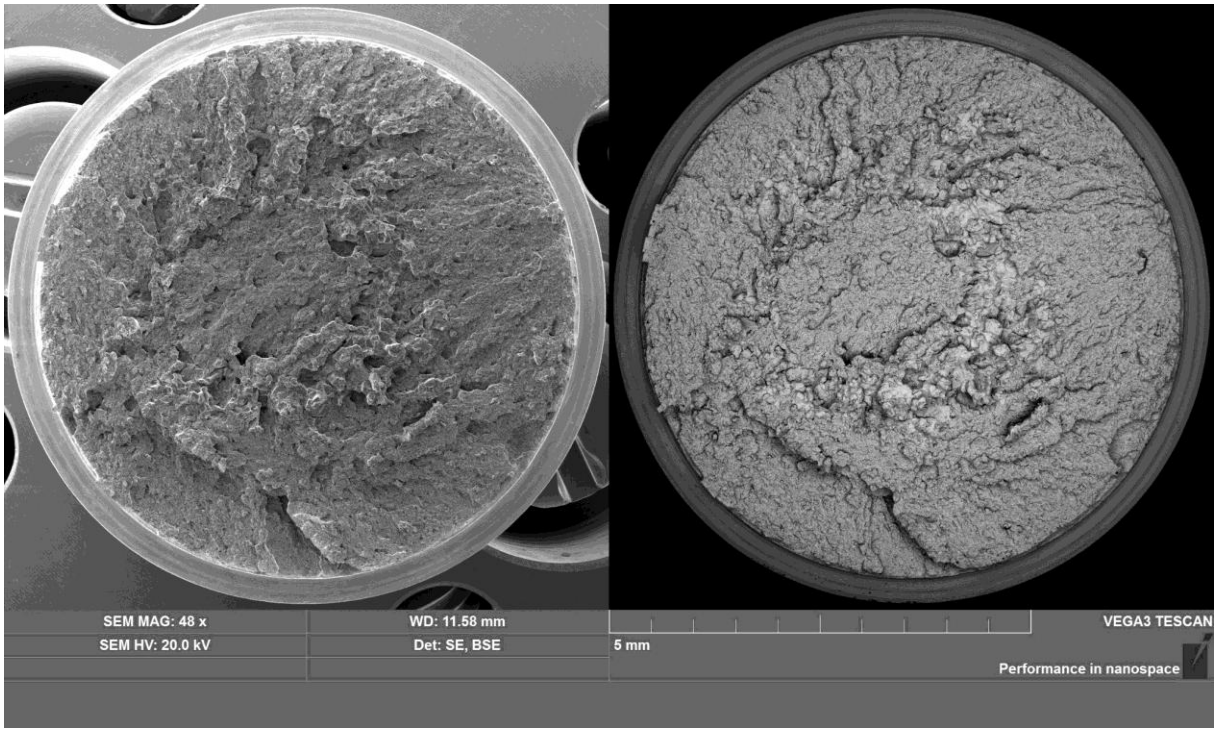

Figure 43 X40CrSiMo 10-2 hydrogen charged samples fracture surface overview.

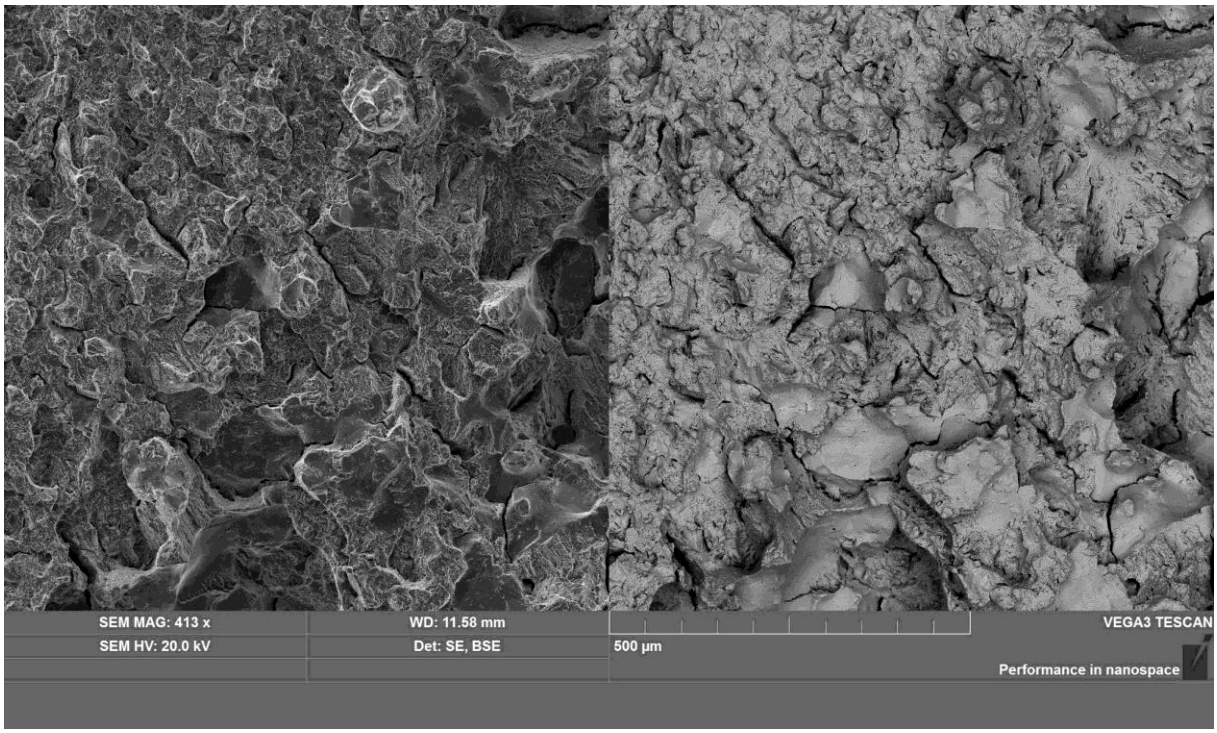

Figure 44 X40CrSiMo 10-2 hydrogen charged samples fracture surface showing some intergranular fracture type.

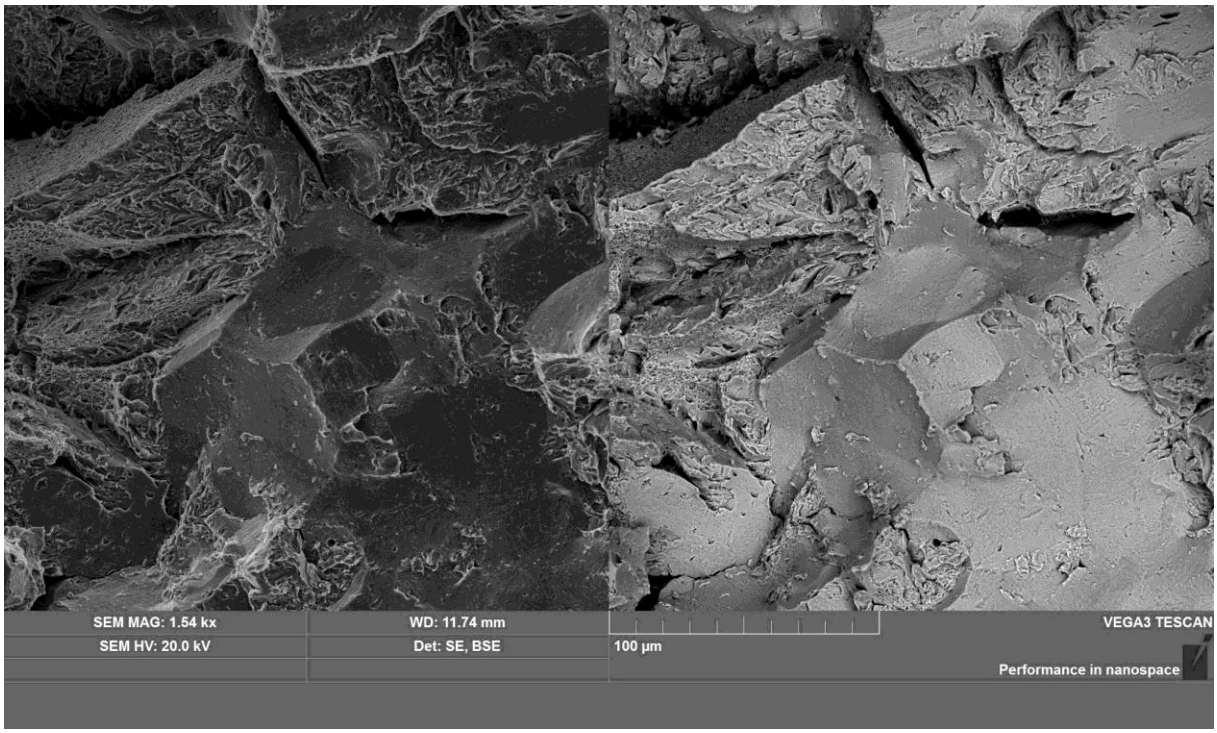

Figure 45 X40CrSiMo 10-2 hydrogen charged samples closer look at the intergranular fracture.

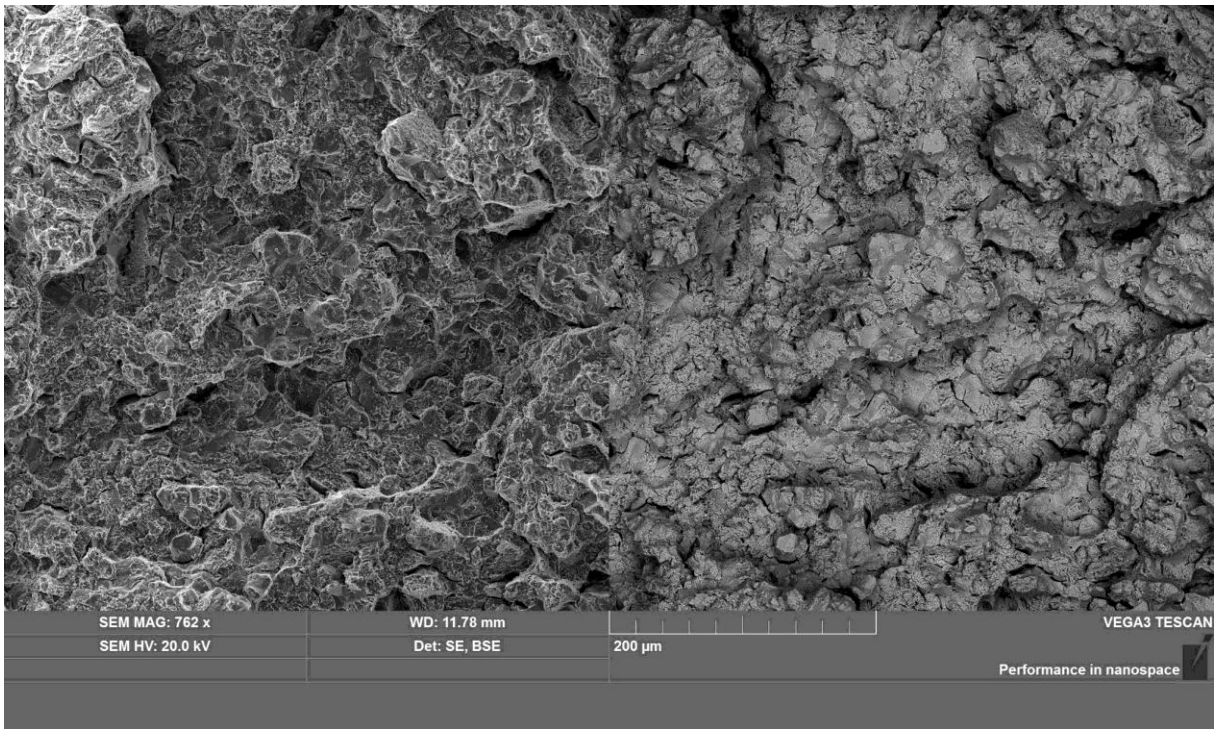

Figure 46 X40CrSiMo 10-2 non-hydrogen charged samples fracture surface.

Overview of the 42CrMo4 non-charged and hydrogen charged samples fracture surfaces can be seen in Figure 47 and Figure 48 respectively. Comparing the two together shows that the non-charged sample has more height than the hydrogen charged one. Based on the tensile testing data it has deformed more in the plastic region of the stress strain curve. Both are indicators for necking of the sample. The area showing the necking is outlined with red. Closeup of both samples fracture type in the red area can be seen in Figure 49 and Figure 50, and it is quasi-cleavage fracture in both. It is a transgranular fracture which happens when there is localized plastic deformation. It is typical for transgranular fracture to show similarities to the microstructure of the material. This could explain why the non-charged sample has a bigger area of it. The fracture type outside red area on the non-charged sample can be seen in Figure 51. Hydrogen charged sample can be seen in Figure 52 and with a higher magnification in Figure 53. Comparing them together the non-charged sample has more dimples, and the dimple size is larger. Also, there are more signs of transgranular brittle fractures on the hydrogen charged sample. As, the martensitic structure could be seen from the higher magnification image.

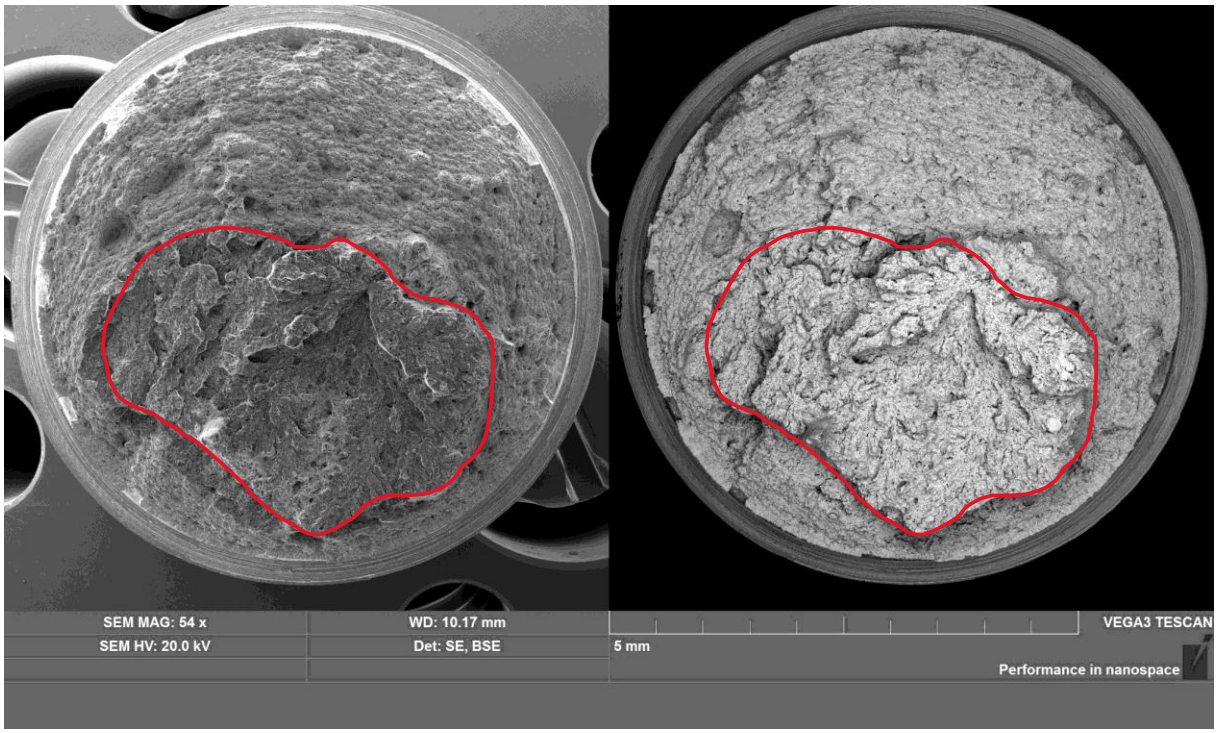

Figure 47 42CrMo4 non-hydrogen charged samples fracture surface overview.

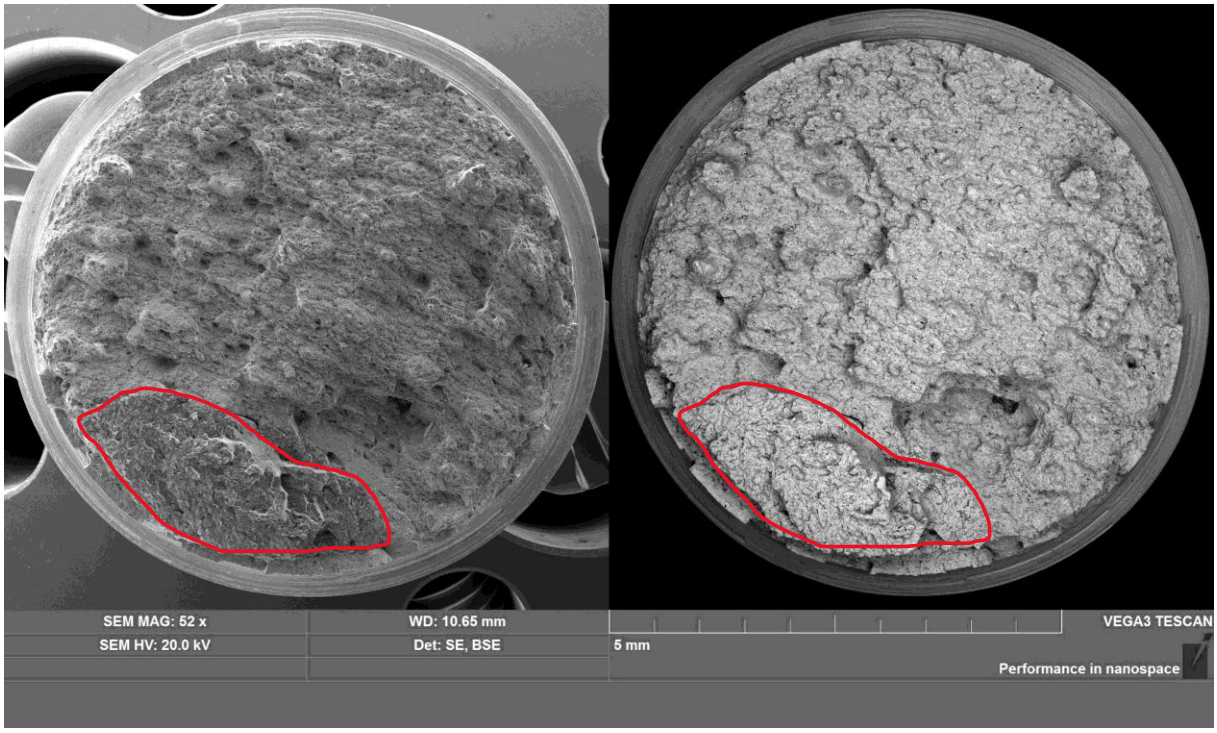

Figure 48 42CrMo4 hydrogen charged samples fracture surface overview.

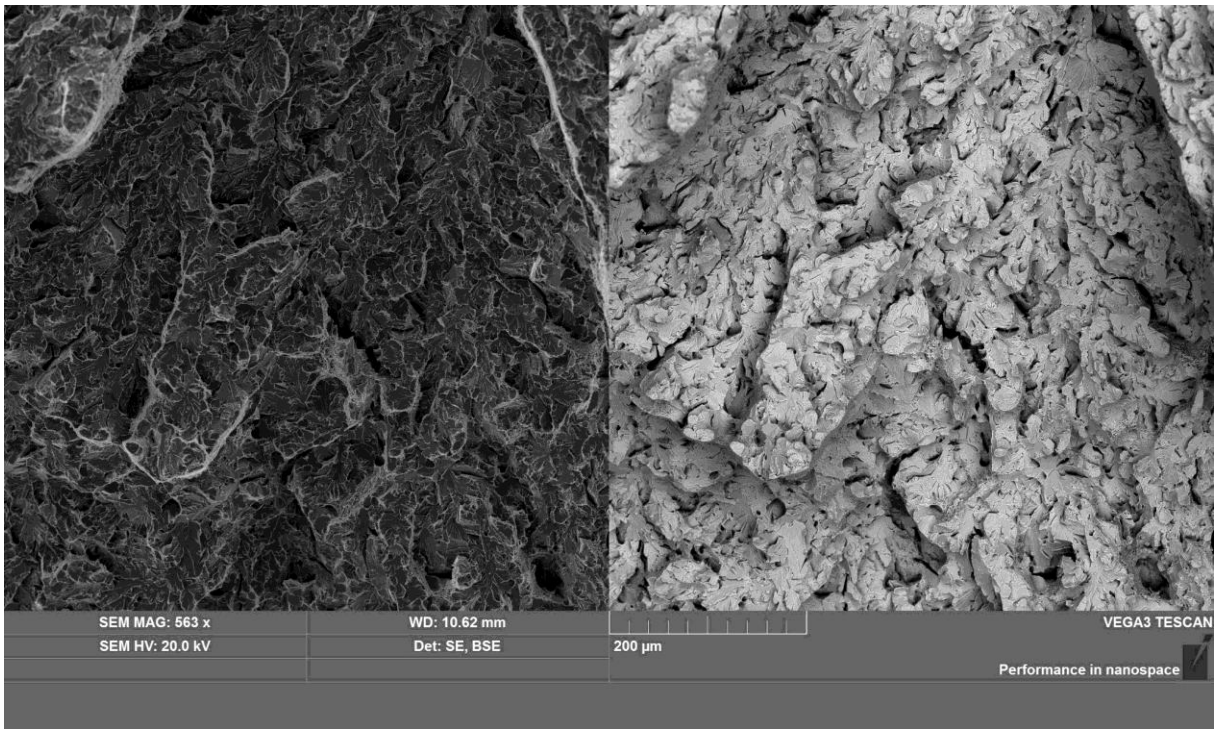

Figure 49 42CrMo4 non-hydrogen charged samples fracture type on the red outlined area.

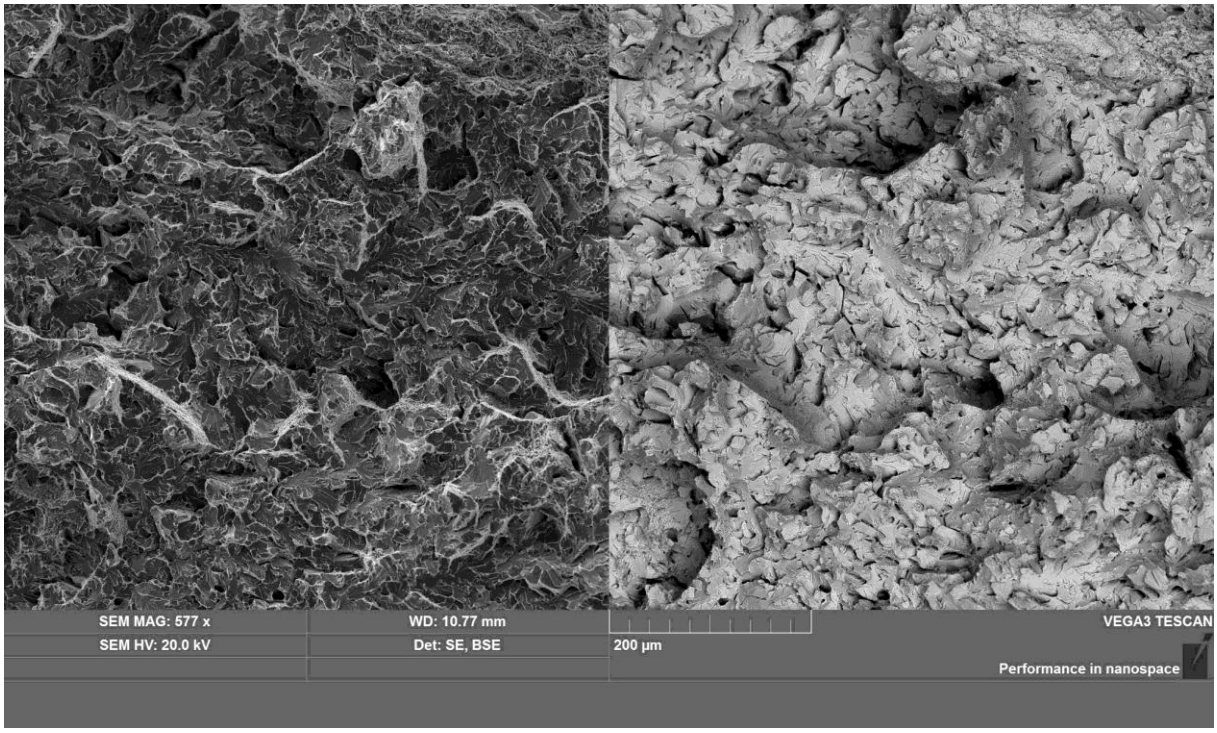

Figure 50 42CrMo4 hydrogen charged samples fracture type on the red outlined area.

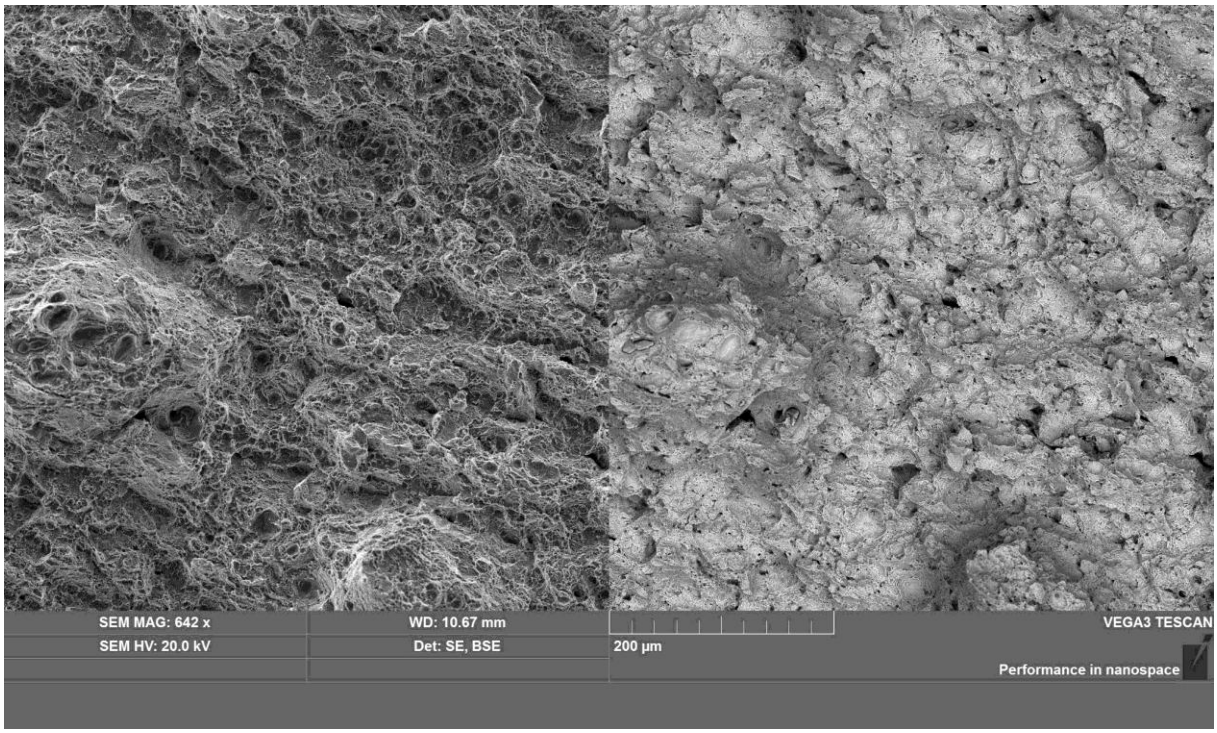

Figure 51 42CrMo4 non-hydrogen charged samples fracture type outside the red area.

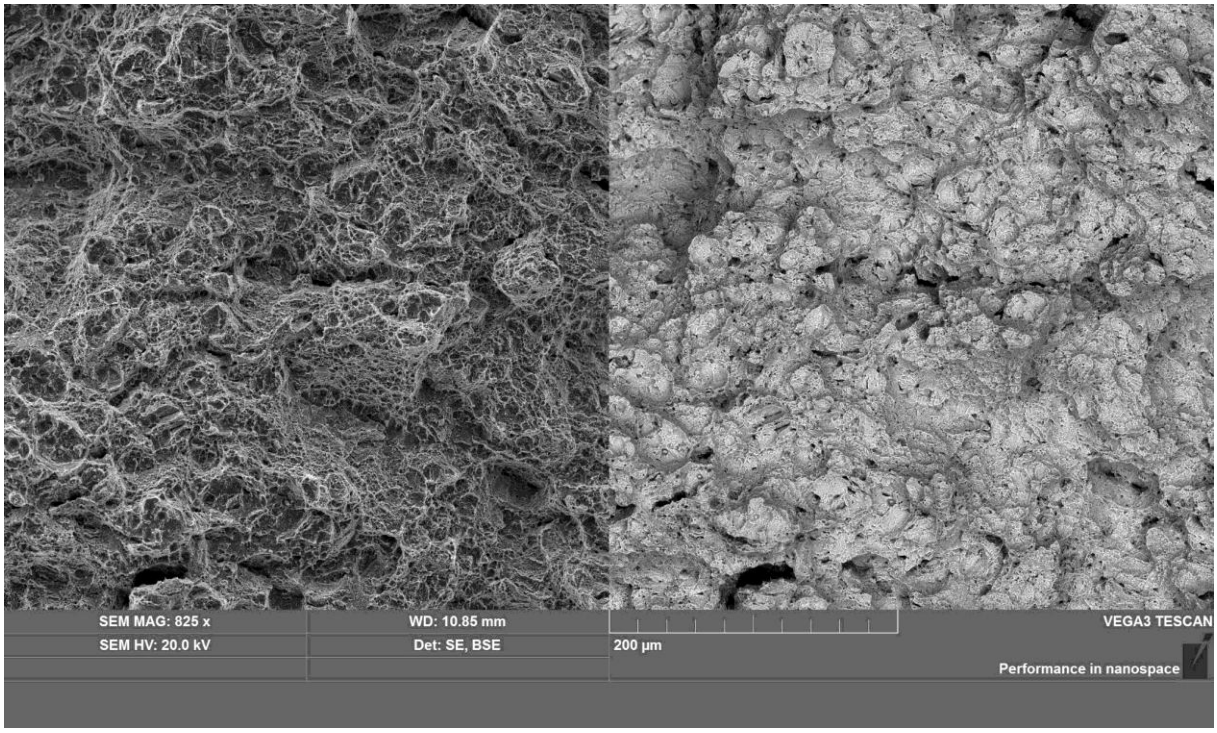

Figure 52 42CrMo4 hydrogen charged samples fracture type outside the red area.

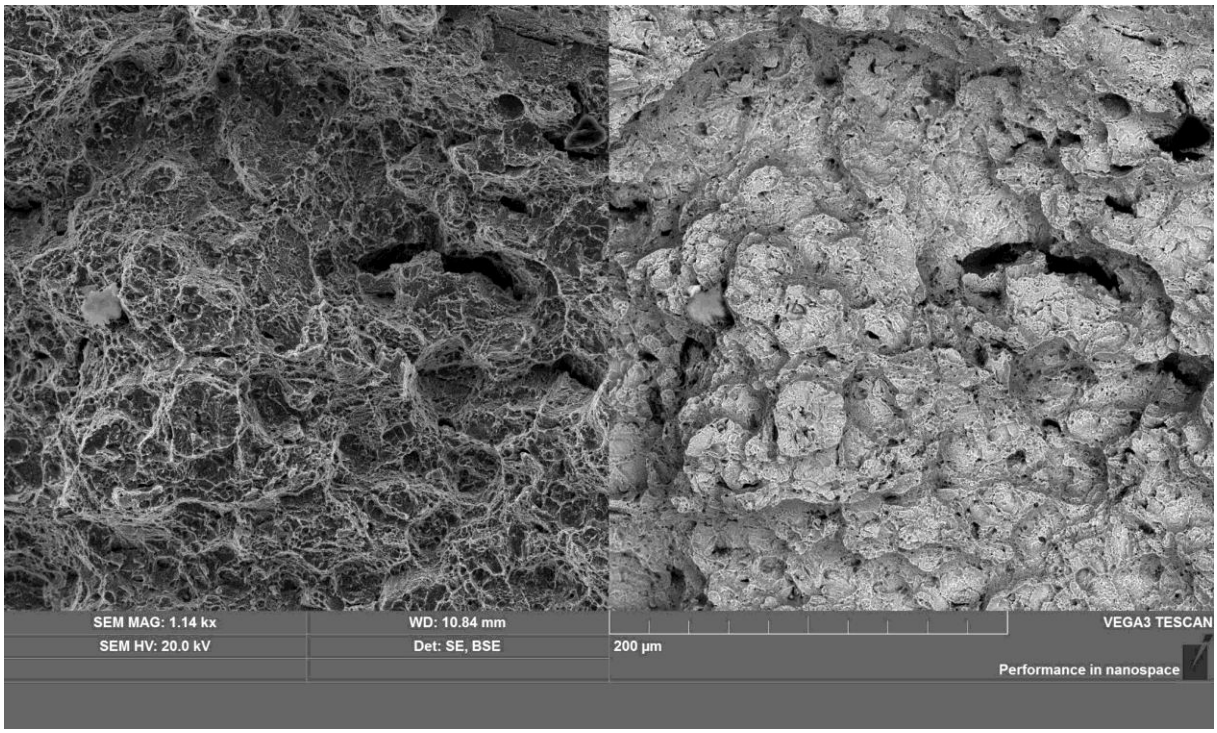

Figure 53 Closer look at 42CrMo4 hydrogen charged samples fracture type outside the red area.

4.6 Possible future developments

The experiment only had one variable, the samples being hydrogen charged or not. It could be beneficial to have more samples with different charging times, to see how the different hydrogen content affects the materials. Also, to have more samples per condition to eliminate the possibility for anomalies. For 42CrMo4 this has already been done in the literature but for X40CrSiMo 10-2 nothing was found. Also, the use of hydrogen gas would better simulate the real atmosphere. The atmosphere inside the cylinder in an internal combustion engine has variation of temperature and pressure. Also, the exposure time would be one variable inside the cylinder. These variables would bring the testing closer to the real atmosphere where the materials operate. These could be varied to obtain a wider range of knowledge for the material inside the engine. As it could be possible for the materials to be more susceptible to hydrogen embrittlement at lower temperatures and higher pressures. As, hydrogen desorbs from metals at higher temperatures.

5 Conclusions

In conclusion, this study aimed to test the mechanical properties of two internal combustion engines component materials in hydrogen atmosphere. These two materials were 42CrMo4 and X40CrSiMo 10-2.

The research in the literature review focused on the hydrogen embrittlement phenomenon and previous findings for 42CrMo4. Also, basic knowledge of hydrogen, internal combustion engines and failure analysis were covered. Potential mitigation possibilities were also mentioned based on other studies.

Two samples were prepared from each material for tensile testing in air and after precharging with hydrogen. They were charged electrochemically in an acidic electrolyte of 1 M H_2SO_4 and 2 g/l of thiourea, with a current density of 1 mA/cm^2 for 6 hours. Tensile testing parameters were room temperature ~21°C and displacement rate of 0,1 mm/min.

The machining, hydrogen charging, and tensile testing were done by the University of Oulu. Tensile testing results showed that both materials were susceptible to hydrogen embrittlement. This was measured with hydrogen embrittlement index (HEI) i.e. the amount of reduction in selected mechanical properties. X40CrSiMo 10-2 HEI% calculated based on fracture point's strength, ultimate tensile strength, strain, and toughness were 6,7%, 6,7%, 60,2%, and 67,7% respectively. For 42CrMo4 the values were -10,3%, 3,3%, 52,1%, and 54,9% respectively. These results would indicate that the biggest impact on the mechanical properties were on strain and toughness. These results are only indicative as there were only one test done per condition. Thus, strength and other results could differ if more tests were done. The toughness reduction could affect the components lifetime, as the material cannot absorb the same amount of energy as the non-hydrogen charged one.

The fracture surfaces also showed signs of hydrogen embrittlement by having more intergranular fractures on the hydrogen-charged X40CrSiMo 10-2 sample. On the hydrogen-charged 42CrMo4 both the dimple size and the area of the fracture surface related to necking were smaller.

References

[1] M. G. Rasul, M. A. Hazrat, M. A. Sattar, M. I. Jahirul, and M. J. Shearer, "The future of hydrogen: Challenges on production, storage and applications," *Energy Convers. Manag.*, vol. 272, p. 116326, Nov. 2022, doi: 10.1016/j.enconman.2022.116326.

[2] L. Bromberg and W. Cheng, "Methanol as an alternative transportation fuel in the US: Options for sustainable and/or energy-secure transportation," Feb. 2015.

[3] A. Franco and C. Giovannini, "Hydrogen Gas Compression for Efficient Storage: Balancing Energy and Increasing Density," *Hydrogen*, vol. 5, no. 2, Art. no. 2, Jun. 2024, doi: 10.3390/hydrogen5020017.

[4] W. Qu, Y. Fang, Z. Wang, H. Sun, and L. Feng, "Optimization of injection system for a medium-speed four-stroke spark-ignition marine hydrogen engine," *Int. J. Hydrog. Energy*, vol. 47, no. 44, pp. 19289–19297, May 2022, doi: 10.1016/j.ijhydene.2022.04.096.

[5] M. M. Hossain Bhuiyan and Z. Siddique, "Hydrogen as an alternative fuel: A comprehensive review of challenges and opportunities in production, storage, and transportation," *Int. J. Hydrog. Energy*, vol. 102, pp. 1026–1044, Feb. 2025, doi: 10.1016/j.ijhydene.2025.01.033.

[6] J. F. Kershaw, *SAE International's Dictionary for Automotive Engineers*. Warrendale: SAE International, 2023. doi: 10.4271/9781468604078.

[7] J. B. Heywood, *Internal combustion engine fundamentals*. in McGraw-Hill series in mechanical engineering. New York: McGraw-Hill, 1988.

[8] Z.-M. Huang, S. Hemeda, and IntechOpen (firm), Eds., *Failure Analysis*. London, United Kingdom: IntechOpen, 2019.

[9] E. Espinel-Blanco, N. Y. Perez-Rangel, and E. Florez-Solano, "Fracture failure analysis of metal materials by visual inspection and destructive testing," *J. Phys. Conf. Ser.*, vol. 2046, no. 1, p. 012060, Oct. 2021, doi: 10.1088/1742-6596/2046/1/012060.

[10] R. Prakash, *Non-destructive testing techniques*, Online-Ausg. Tunbridge Wells: New Academic Science, 2012.

[11] P. J. Potts and M. West, Eds., *Portable x-ray fluorescence spectrometry: capabilities for in situ analysis*. Cambridge, UK: RSC Pub, 2008.

[12] H. Yu *et al.*, "Hydrogen Embrittlement as a Conspicuous Material Challenge─Comprehensive Review and Future Directions," *Chem. Rev.*, vol. 124, no. 10, pp. 6271–6392, May 2024, doi: 10.1021/acs.chemrev.3c00624.

[13] J. R. Davis, Ed., *Tensile testing*, 2nd ed. Materials Park, Ohio: ASM International, 2010.

[14] S. Thomas, R. A. Shanks, and S. Chandrasekharakurup, Eds., *Design and applications of nanostructured polymer blends and nanocomposite systems*. in Micro & nano technologies series. Amsterdam Boston Heidelberg: Elsevier, William Andrew, 2016.

[15] M. Boåsen, C. F. O. Dahlberg, P. Efsing, and J. Faleskog, "A weakest link model for multiple mechanism brittle fracture — Model development and application," *J. Mech. Phys. Solids*, vol. 147, p. 104224, Feb. 2021, doi: 10.1016/j.jmps.2020.104224.

[16] A. Hojná, "Overview of Intergranular Fracture of Neutron Irradiated Austenitic Stainless Steels," *Metals*, vol. 7, no. 10, p. 392, Oct. 2017, doi: 10.3390/met7100392.

[17] "(PDF) Hydrogen effects on fracture of high-strength steels with different micro-alloying," ResearchGate. Accessed: Oct. 03, 2025. [Online]. Available: https://www.researchgate.net/publication/281104598_Hydrogen_effects_on_fracture_of_high-strength_steels_with_different_micro-alloying

[18] Schroeder Craig J.; Parrington Ronald J.; Maciejewski Joseph O.; Lane James F., *ASM Handbook Volume 12 - Fractography*. ASM International, 2024.

[19] "(PDF) Microfracture maps in progressively drawn pearlitic steels under triaxial stress states," *ResearchGate*, Aug. 2025, doi: 10.1504/IJMATEI.2009.024027.

[20] "(PDF) Experimental and Finite Element Analyses on Stress Intensity Factors of an Elliptical Surface Crack in a Circular Shaft Under Tension and Bending," *ResearchGate*, Aug. 2025, doi: 10.1023/B:FRAC.0000047784.23236.7d.

[21] S. Ono *et al.*, "A Heterothermic Kinetic Model of Hydrogen Absorption in Metals with Subsurface Transport," *Metals*, vol. 9, no. 10, Art. no. 10, Oct. 2019, doi: 10.3390/met9101131.

[22] X. Li, X. Ma, J. Zhang, E. Akiyama, Y. Wang, and X. Song, “Review of Hydrogen Embrittlement in Metals: Hydrogen Diffusion, Hydrogen Characterization, Hydrogen Embrittlement Mechanism and Prevention,” *Acta Metall. Sin. Engl. Lett.*, vol. 33, no. 6, pp. 759–773, Jun. 2020, doi: 10.1007/s40195-020-01039-7.
[23] “ASM handbook. 9: Metallography and microstructures,” 1. print., Materials Park, Ohio: ASM International, 2004.
[24] M. Koyama *et al.*, “Recent progress in microstructural hydrogen mapping in steels: Quantification, kinetic analysis, and multi-scale characterisation,” *Mater. Sci. Technol.*, vol. 33, no. 13, pp. 1481–1496, Sep. 2017, doi: 10.1080/02670836.2017.1299276.
[25] T. Michler and M. P. Balogh, “Hydrogen environment embrittlement of an ODS RAF steel – Role of irreversible hydrogen trap sites,” *Int. J. Hydrog. Energy*, vol. 35, no. 18, pp. 9746–9754, Sep. 2010, doi: 10.1016/j.ijhydene.2010.06.071.
[26] L. Fu and H. Fang, “Formation Criterion of Hydrogen-Induced Cracking in Steel Based on Fracture Mechanics,” *Metals*, vol. 8, no. 11, Art. no. 11, Nov. 2018, doi: 10.3390/met8110940.
[27] S. Lynch, “Hydrogen embrittlement phenomena and mechanisms,” *Corros. Rev.*, vol. 30, no. 3–4, pp. 105–123, Jun. 2012, doi: 10.1515/corrrev-2012-0502.
[28] H. Matsunaga, *Hydrogen Gas Embrittlement: Mechanisms, Mechanics, and Design*. Amsterdam: Elsevier, 2024.
[29] Y.-S. Chen *et al.*, “Hydrogen trapping and embrittlement in metals – A review,” *Int. J. Hydrog. Energy*, vol. 136, pp. 789–821, Jun. 2025, doi: 10.1016/j.ijhydene.2024.04.076.
[30] H. K. Birnbaum and P. Sofronis, “Hydrogen-enhanced localized plasticity—a mechanism for hydrogen-related fracture,” *Mater. Sci. Eng. A*, vol. 176, no. 1, pp. 191–202, Mar. 1994, doi: 10.1016/0921-5093(94)90975-X.
[31] “(PDF) Overview of hydrogen-resistant alloys for high-pressure hydrogen environment: on the hydrogen energy structural materials,” *ResearchGate*, doi: 10.1093/ce/zkad009.
[32] T. Neeraj, R. Srinivasan, and J. Li, “Hydrogen embrittlement of ferritic steels: Observations on deformation microstructure, nanoscale dimples and failure by nanovoiding,” *Acta Mater.*, vol. 60, no. 13, pp. 5160–5171, Aug. 2012, doi: 10.1016/j.actamat.2012.06.014.
[33] J. A. Lee and S. Woods, “Hydrogen Embrittlement,” JSC-CN-36009, Apr. 2016. Accessed: Jul. 14, 2025. [Online]. Available: https://ntrs.nasa.gov/citations/20160005654
[34] C. San Marchi, B. P. Somerday, X. Tang, and G. H. Schiroky, “Effects of alloy composition and strain hardening on tensile fracture of hydrogen-precharged type 316 stainless steels,” *Int. J. Hydrog. Energy*, vol. 33, no. 2, pp. 889–904, Jan. 2008, doi: 10.1016/j.ijhydene.2007.10.046.
[35] C. L. Lai, L. W. Tsay, and C. Chen, “Effect of microstructure on hydrogen embrittlement of various stainless steels,” *Mater. Sci. Eng. A*, vol. 584, pp. 14–20, Nov. 2013, doi: 10.1016/j.msea.2013.07.004.
[36] G. A. Martiniano, W. W. Bose Filho, R. P. Garcia, and S. D. Franco, “Temperature effect on hydrogen embrittlement susceptibility of a high strength martensitic steel,” *Int. J. Hydrog. Energy*, vol. 110, pp. 457–469, Mar. 2024, doi: 10.1016/j.ijhydene.2025.02.253.
[37] S. K. Lawrence and J. P. Wharry, “Hydrogen Effects on Material Performance,” *JOM*, vol. 72, no. 5, pp. 1979–1981, May 2020, doi: 10.1007/s11837-020-04123-6.
[38] K. Saito and K. Takai, “Hydrogen Desorption Behavior Trapped in Various Microstructures of High-Strength Steels Using Thermal Desorption Analysis,” *Metall. Mater. Trans. A*, vol. 52, no. 2, pp. 531–543, Feb. 2021, doi: 10.1007/s11661-020-06096-2.
[39] X. Xing *et al.*, “Quantification of the temperature threshold of hydrogen embrittlement in X90 pipeline steel,” *Mater. Sci. Eng. A*, vol. 800, p. 140118, Jan. 2021, doi: 10.1016/j.msea.2020.140118.
[40] L. Cho *et al.*, “Effects of hydrogen pressure and prior austenite grain size on the hydrogen embrittlement characteristics of a press-hardened martensitic steel,” *Int. J. Hydrog. Energy*, vol. 46, no. 47, pp. 24425–24439, Jul. 2021, doi: 10.1016/j.ijhydene.2021.05.005.
[41] K. Koide, T. Minami, T. Anraku, A. Iwase, and H. Inoue, “Effect of Hydrogen Partial Pressure on the Hydrogen Embrittlement Susceptibility of Type304 Stainless Steel in High-pressure H2/Ar Mixed Gas,” *ISIJ Int.*, vol. 55, no. 11, pp. 2477–2482, 2015, doi: 10.2355/isijinternational.ISIJINT-2015-232.

[42] H.-J. Wan, X.-Q. Wu, H.-L. Ming, J.-Q. Wang, and E.-H. Han, "Effects of Hydrogen Charging Time and Pressure on the Hydrogen Embrittlement Susceptibility of X52 Pipeline Steel Material," *Acta Metall. Sin. Engl. Lett.*, vol. 37, no. 2, pp. 293–307, Feb. 2024, doi: 10.1007/s40195-023-01625-5.
[43] V. Arniella, A. Zafra, G. Álvarez, J. Belzunce, and C. Rodríguez, "Comparative study of embrittlement of quenched and tempered steels in hydrogen environments," *Int. J. Hydrog. Energy*, vol. 47, no. 38, pp. 17056–17068, May 2022, doi: 10.1016/j.ijhydene.2022.03.203.
[44] A. Imdad and F. J. B. Varela, "In-Situ Hydrogen Charging Effect on the Fracture Behaviour of 42CrMo4 Steel Submitted to Various Quenched and Tempering Heat Treatments," *Hydrogen*, vol. 4, no. 4, Art. no. 4, Dec. 2023, doi: 10.3390/hydrogen4040060.
[45] A. Zafra, L. B. Peral, J. Belzunce, and C. Rodríguez, "Effect of hydrogen on the tensile properties of 42CrMo4 steel quenched and tempered at different temperatures," *Int. J. Hydrog. Energy*, vol. 43, no. 18, pp. 9068–9082, May 2018, doi: 10.1016/j.ijhydene.2018.03.158.
[46] P. Zhou, W. Li, X. Zhu, Y. Li, X. Jin, and J. Chen, "Graphene Containing Composite Coatings as a Protective Coatings against Hydrogen Embrittlement in Quenching & Partitioning High Strength Steel," *J. Electrochem. Soc.*, vol. 163, no. 5, p. D160, Jan. 2016, doi: 10.1149/2.0551605jes.
[47] T.-H. Nam, J.-H. Lee, S.-R. Choi, J.-B. Yoo, and J.-G. Kim, "Graphene coating as a protective barrier against hydrogen embrittlement," *Int. J. Hydrog. Energy*, vol. 39, no. 22, pp. 11810–11817, Jul. 2014, doi: 10.1016/j.ijhydene.2014.05.132.
[48] A. Imdad, V. Arniella, A. Zafra, and J. Belzunce, "Tensile behaviour of 42CrMo4 steel submitted to annealed, normalized, and quench and tempering heat treatments with in-situ hydrogen charging," *Int. J. Hydrog. Energy*, vol. 50, pp. 270–280, Jan. 2024, doi: 10.1016/j.ijhydene.2023.10.082.
[49] "OES-PO41283-OES-quick-guide.pdf." Accessed: Sep. 24, 2025. [Online]. Available: https://documents.thermofisher.com/TFS-Assets/MSD/posters/OES-PO41283-OES-quick-guide.pdf
[50] "VS3004_Haertepruefung_uebersicht_Poster_01.03.2021_01.pdf." Accessed: Sep. 24, 2025. [Online]. Available: https://api.emcotest.com/static/downloads/VS3004_Haertepruefung_uebersicht_Poster_01.03.2021_01.pdf
[51] "Scanning Electron Microscopy | Principles of Scanning Electron Microscopy - FI." Accessed: Oct. 01, 2025. [Online]. Available: https://www.thermofisher.com/uk/en/home/materials-science/learning-center/applications/scanning-electron-microscope-sem-electron-column.html